INL/RPT-22-68666
Revision 0

Microstructural Characterization of A709 Commercial Heats with Precipitation Treatment

August 2022

Ninad Mohale
Idaho National Laboratory

Ryann Bass
Idaho National Laboratory

Idaho National Laboratory

INL is a U.S. Department of Energy National Laboratory
operated by Battelle Energy Alliance, LLC

INL/RPT-22-68666
Revision 0

Microstructural Characterization of A709 Commercial Heats with Precipitation Treatment

Ninad Mohale
Idaho National Laboratory
Ryann Bass
Idaho National Laboratory

August 2022

Idaho National Laboratory
Advanced Reactor Technologies
Idaho Falls, Idaho 83415

http://www.inl.gov

Prepared for the
U.S. Department of Energy
Office of Nuclear Energy
Under DOE Idaho Operations Office
Contract DE-AC07-05ID14517

Page intentionally left blank

INL ART Program

Microstructural Characterization of A709 Commercial Heats with Precipitation Treatment

INL/EXT-22-68666
Revision 0
August 2022

Technical Reviewer: (Confirmation of mathematical accuracy, and correctness of data and appropriateness of assumptions.)

Michael D. McMurtrey ART Elevated-Temperature Metals Lead	8/17/2022 Date

Approved by:

M. Davenport Michael E. Davenport ART Project Manager	8/17/2022 Date
Travis Mitchell Travis R. Mitchell ART Program Manager	8/17/2022 Date
Michelle Sharp Michelle T. Sharp INL Quality Assurance	8/17/2022 Date

Page intentionally left blank

SUMMARY

This report discusses work conducted at Idaho National Laboratory in fiscal year 2022 associated with the precipitates in Alloy 709 (A709). The purpose of this work is to support the development of the A709 Code Cases to qualify A709 in Section III, Division 5 of the American Society of Mechanical Engineers Boiler and Pressure Vessel Code. This would permit the use of A709 for elevated-temperature nuclear construction. This work encompassed two broad goals. The first goal was to understand the microstructure of the second Commercial Heat of plate A709 purchased through the Advanced Reactors Technologies Program in both the solution-annealed and precipitation-treated conditions. Transmission electron microscopy was utilized to characterize these microstructures. Direct comparisons were then made between the solution-annealed and precipitation-treated conditions as well as between the first and second Commercial Heats of plate A709. The second goal was to understand the impact of variations in the time and temperature of the precipitation treatment on the properties of A709. The precipitation treatment temperature was varied from 750°C to 800°C for times ranging from 3 hours to 30 hours. The hardness of each precipitation treatment variation was measured. All the precipitation treatment variations investigated met the room-temperature hardness requirement specified in American Society for Testing and Materials (ASTM) A213 and solution annealed (SA)-213 for UNS S31025 except a specimen from the second Commercial Heat of plate A709 precipitation-treated at 800°C for 9 hours. The hardness measured for the specimen from the second Commercial Heat of plate A709 that was precipitation-treated at 800°C for 9 hours is considered an outlier. The next step is to look at the extremes of the precipitation treatment variations investigated and conduct elevated-temperature mechanical testing. The purpose of this testing would be to assess if these time and temperature variations have any impact on the mechanical performance.

Page intentionally left blank

ACKNOWLEDGEMENTS

This research was sponsored by the United States (U.S.) Department of Energy (DOE) under Contract No. DE-AC07-05ID14517 with Idaho National Laboratory (INL), which is managed and operated by Battelle Energy Alliance. Programmatic direction was provided by the Office of Nuclear Reactor Deployment of the DOE Office of Nuclear Energy.

The authors gratefully acknowledge the support provided by Sue Lesica, Federal Lead for Advanced Materials, Advanced Reactor Technologies (ART) Program; Brian Robinson, Federal Manager, ART Fast Reactors (FR) Campaign; Bo Feng, Argonne National Laboratory, National Technical Director, ART FR Campaign; and Ting-Leung Sham, INL, ART Advanced Materials Technology Area Lead.

The authors acknowledge helpful discussions with Richard Wright, Structural Alloys, LLC; Ting-Leung Sham, INL; Michael McMurtrey, INL; Xuan Zhang, Argonne National Laboratory (ANL); Yanli Wang, Oak Ridge National Laboratory (ORNL); and Grace Burke, ORNL. The authors also thank J. Wesley Jones and Joel A. Simpson of INL for their assistance.

Page intentionally left blank

CONTENTS

Figures

Tables

Page intentionally left blank

ACRONYMS

A709	Alloy 709
ANL	Argonne National Laboratory
AOD	argon oxygen decarburization
ART	Advanced Reactor Technologies
ASME	American Society of Mechanical Engineers
ASTM	American Society for Testing and Materials
ATI	Allegheny Technologies Incorporated
BF	bright field
BPVC	Boiler and Pressure Vessel Code
DF	dark field
DOE	U.S. Department of Energy
EDS	energy dispersive spectroscopy
ESR	electroslag remelting
FR	Fast Reactors
FY	fiscal year
INL	Idaho National Laboratory
NRC	U.S. Nuclear Regulatory Commission
ORNL	Oak Ridge National Laboratory
PT	precipitation-treated
SA	solution annealed
SFR	sodium-cooled fast reactor
SS	stainless steel
STEM	scanning transmission electron microscopy
TEM	transmission electron microscopy
TTT	time-temperature-transformation
U.S.	United States

Page intentionally left blank

1. MOTIVATION

President Biden's Executive Order 14008 issued a federal directive for the development of a plan to facilitate a carbon-zero electric-industry sector by 2035 (Exec. Order No. 14008 2021). Nuclear energy is one potential resource to satisfy this executive order. One of the leading advanced nuclear reactor concepts is the sodium-cooled fast reactor (SFR). Other needs not associated with this executive order, but important for clean energy—such as the recycling of spent nuclear fuel—can also be attained with SFRs (Sham and Natesan 2017).

SFR commercialization is dependent upon these reactors being economically viable. A crucial aspect to achieving this commercialization is qualifying advanced materials for nuclear reactor use, which can reduce capital constructions costs. Although advanced materials are typically more expensive than traditional steels, they offer advantages that may ultimately lead to savings. Advanced materials may enable higher operating temperatures, which improves thermal efficiency and leads to increased power output. Additionally, advanced materials may offer longer design lifetimes, meaning components may not have to be replaced as often. Besides economic savings, advanced materials may offer improved safety margins, material reliability, and design flexibility (Sham and Natesan 2017).

Alloy 709 (A709), an austenitic stainless steel (SS), has been identified as an advanced material that would improve the viability of SFRs. A709 has better creep properties than 316H SS, the reference construction material for SFRs, but is not as expensive as nickel-based alloys usually used at high temperatures. This enables the construction of components with thinner walls, reducing construction costs. A709 has an improved resistance to thermal gradients compared to 316H SS. This eliminates the need for the expensive add-on hardware required for construction with 316H SS, further reducing construction costs. Potential SFR components to be constructed with A709 are the reactor vessel, piping, core supports, intermediate heat exchanger, and compact heat exchanger. The compact heat exchanger could link the SFR to a supercritical carbon dioxide Brayton energy conversion system as one possible application (Sham and Natesan 2017).

In the United States (U.S.), the U.S. Nuclear Regulatory Commission (NRC) licenses and regulates nuclear reactors and nuclear reactor designs. Nuclear plant owners and operators can take advantage of Section III, Division 5 of the American Society of Mechanical Engineers (ASME) Boiler and Pressure Vessel Code (BPVC) to reduce the effort needed to license a nuclear reactor or nuclear reactor design. This section of the Code provides design rules for elevated-temperature nuclear construction (ASME 2021a). The NRC is in the process of evaluating the 2017 version of Section III, Division 5 for potential endorsement (Thomas 2018; Nuclear Regulatory Commission 2022). A709 is currently not qualified in Section III, Division 5 of the ASME BPVC. Three U.S. Department of Energy (DOE) national laboratories—Argonne National Laboratory (ANL), Idaho National Laboratory (INL), and Oak Ridge National Laboratory (ORNL)—are collaborating on a program to qualify A709 in Section III, Division 5 of the ASME BPVC through multiple Code Cases. The purpose of this report is to discuss work conducted at INL in fiscal year (FY) 2022 associated with A709 precipitates to support the A709 Code Cases. A more thorough description of this work is provided in Section 3.

2. BACKGROUND

2.1 A709

A709 is an austenitic SS that is based on NF709 which was developed by Nippon Steel and Sumitomo Metal Corporation as a tubing material for ultra-supercritical boiler applications. NF709 was designed so that detrimental intermetallics do not precipitate during long-term, elevated-temperature service (Sham and Natesan 2017). NF709 is included in the American Society for Testing and Materials (ASTM) specification A213 and ASME specification solution annealed (SA)-213. Both specifications are entitled "Standard Specification for Seamless Ferritic and Austenitic Alloy-Steel Boiler, Superheater, and Heat Exchanger Tubes." NF709 is designated as grade TP310MoCbN and UNS S31025 (ASTM 2021a; ASME 2021b). ASME BPVC Case 2581 qualifies the construction of NF709 seamless tubes for temperatures up to 815°C (1500°F) for Section I applications (ASME 2021c).

A collaboration between ANL, INL, and ORNL was initiated in 2013 to develop A709 plate and characterize its properties. This work resulted in the recommendation to qualify A709 in Section III, Division 5 of the ASME BPVC for elevated-temperature nuclear construction. This recommendation was based on the following findings: (a) A709 is stable in an elevated-temperature, liquid-sodium environment; (b) A709 can be successfully welded with Alloy 625 or optimized A709 filler metals by automated gas-tungsten arc welding; (c) the production of A709 can be optimized to improve the creep-fatigue properties while maintaining creep strength; and (d) the properties of A709 are improved compared to 316H SS, which is qualified in Section III, Division 5 of the ASME BPVC (Sham and Natesan 2017).

A plan for developing the data package needed to qualify A709 in Section III, Division 5 of the ASME BPVC was formulated. Multiple data packages were devised through a staged qualification approach for A709 to support multiple Code Cases with increasing design lives. This approach entails qualifying a material for a shorter design life initially using data that can be generated in the near term. The qualified design life is extended later, once the longer-term data needed to support this extension, such as creep and thermal aging, becomes available. This will enable accelerated qualification of A709. The alternative, non-accelerated approach, is to wait until all necessary data to support a Code Case for the longest design life is generated. This plan took into consideration the needs of both the ASME BPVC and NRC (Sham and Natesan 2017). This includes Nonmandatory Appendix HBB-Y in Section III, Division 5 of the ASME BPVC, which provides guidelines for qualifying new materials, as well as re-occurring issues flagged by the NRC (Sham and Natesan 2017; ASME 2021a; O'Donnell and Griffin 2007). Nonmandatory Appendix HBB-Y specifies that the data package for qualifying new materials must be comprised of data from a minimum of three heats, which need to encompass the composition range, product forms, and size of the components to be used in service (ASME 2021a). It was determined that plate would be the first product form qualified.

The first Commercial Heat of A709 was procured in FY 2017 from Electralloy/G.O. Carlson, heat 58776. This heat was in the plate-product form with the chemical composition provided in Table 1. This heat was procured in a manner that enabled the final processing step and the solution-annealing temperature to be independently investigated. The final processing step was either argon oxygen decarburization (AOD), electroslag remelting (ESR), or ESR with a homogenization treatment (ESR + HOMO). The plates were SA at 1050°C (1922°F), 1100°C (2012°F), or 1150°C (2102°F). A total of nine unique groups of plates were fabricated, one for each processing combination (Natesan et al. 2017). Creep, fatigue, and creep-fatigue testing were initiated to down-select the final processing step and solution-anneal temperature. Plates that were SA at 1050°C (1922°F) were eliminated from consideration because of a too fine grain size and an unacceptably short creep-rupture lifetime. The ESR final processing condition resulted in longer elongations prior to failure during creep, establishing it as the best method of manufacturing. A tradeoff between creep and creep-fatigue properties was found between the solution-annealing temperatures. The plate with the ESR final processing step, SA at 1150°C (2102°F)

had the best creep-rupture properties but inadequate creep-fatigue properties. The processing condition that resulted in the optimal balance in properties was the ESR plate SA at 1100°C (2012°F), although the creep-fatigue properties were worse than desired (McMurtrey 2018; McMurtrey and Rupp 2019; Natesan, Zhang, and Li 2018; Wang et al. 2018).

Table 1. Chemical composition (in wt. %) of the first Commercial Heat of A709 ingot, heat #: 58776-1R.

C	Mn	Si	P	S	Cr	Ni	Mo
0.066	0.9	0.39	0.014	0.001	20.06	25.12	1.5

N	Nb	Ti	Cu	Co	Al	B	Fe
0.16	0.26	0.02	0.06	0.02	0.02	0.0035	Balance

A precipitation treatment for A709 was developed in FY 2019 and emanated from two questions. The first was concerning if the beneficial precipitates that form during accelerated testing would form during service at low temperature, low stress conditions. The second was if the A709 properties, particularly the creep-fatigue properties, could be further improved. Precipitate treating A709 prior to service would ensure that the beneficial precipitates would be present during service conditions. The precipitate treatment needed to precipitate the beneficial MX (Nb, Ti, V: C, N) and Z-phase (CrNbN) without forming the detrimental intermetallics (Fe2Mo, Fe2Nb). A 10-hour, 775°C (1427°F) heat treatment protocol followed by air cooling was identified (Zhang, Sham, and Young 2019). This heat treatment protocol is referred to as a precipitation treatment. This precipitate treatment promoted the precipitation of the beneficial MX and Z-phase and was observed to improve creep-fatigue properties without significantly impacting creep properties (Rupp and McMurtrey 2020). A709 with the ESR final processing step, SA at 1150°C, and precipitation-treated was identified as resulting in the best balance in properties (Sham et al. 2022).

In previous fiscal years, the precipitates present in the Carlson Heat with the ESR final processing step and SA at 1150°C, identified as Commercial Heat 1, in both the SA and precipitation-treated (PT) conditions were characterized (Zhang and Sham 2020; Zhang, Sham and Li 2021; Song, Clement, and McMurtrey 2021). A summary of these findings is provided in Section 2.2. In FY 2021, the impact of variations in the precipitation treatment on the microstructure and properties of A709 was investigated (Song, Clement, and McMurtrey 2021). This work evaluated two variations of the precipitation treatment: (a) a 10-hour, 775°C (1427°F) heat treatment protocol followed by air cooling and (b) a 100-hour, 775°C (1427°F) heat treatment protocol followed by air cooling. The precipitate treatment variations investigated show only slight variations in the microstructure with no difference observed in the room-temperature tensile properties. (Song, Clement, and McMurtrey 2021).

The second Commercial Heat of A709 was ordered in FY 2020 and received in FY 2021 from Allegheny Technologies Incorporated (ATI) Flat Rolled Products in the plate-product form, heat 529900 (Wright 2020). This heat, identified as Commercial Heat 2, was comprised of nine plates, all fabricated by ESR. Of these plates, eight were hot-rolled and SA; six of the plates were nominally 1.75 inches thick and the remining two were nominally 2.0 inches thick. The solution anneal was conducted at a minimum of 1149°C (2100°F). The remaining plate was nominally 1.75 inches thick and delivered in the hot-rolled condition.

2.2 Precipitates Present in Commercial Heat 1

2.2.1 Commercial Heat 1 – SA

Commercial Heat 1 – SA was characterized using transmission electron microscopy (TEM). A bright field (BF) TEM image of the microstructure is shown in Figure 1. Commercial Heat 1 – SA is comprised of dislocations with a density of 2×10^{12} m^{-2} and the precipitate MX. The MX precipitate composition is (Nb, Ti: C, N), and the distribution of the MX precipitate size is shown in Figure 2. MX is face-centered cubic with a lattice parameter slightly greater than austenite. The grain boundaries and the twin boundaries in Commercial Heat 1 – SA are free of secondary phases (Zhang, Sham, and Li 2021).

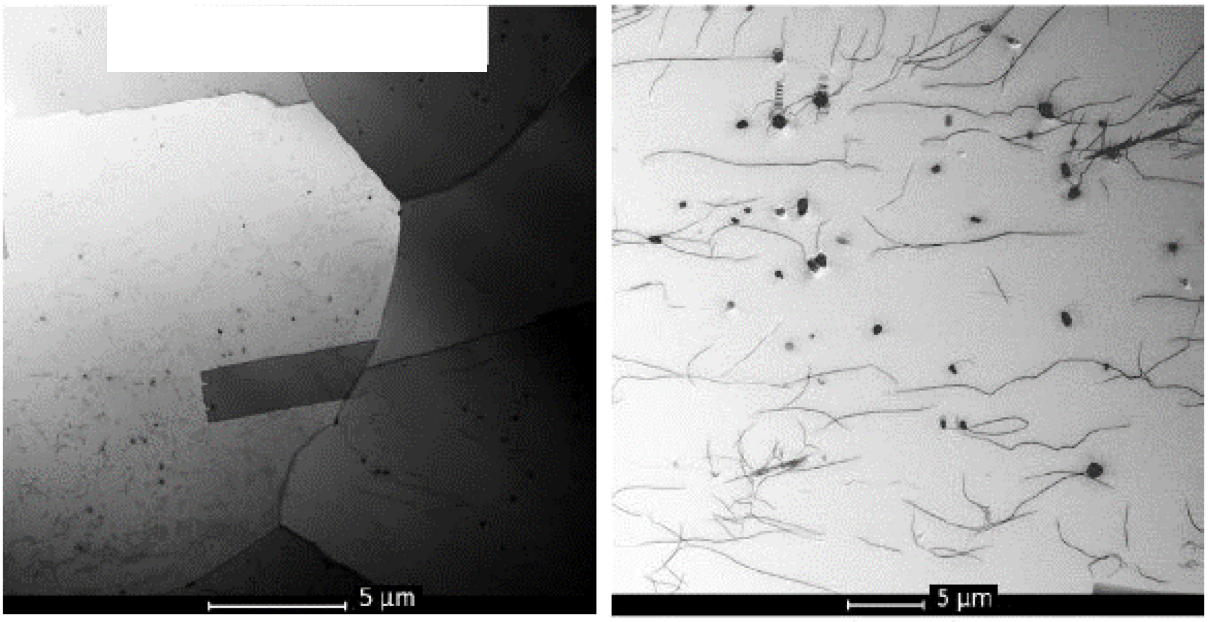

Figure 1. TEM-BF image showing the microstructure of Commercial Heat 1 – SA. The particles in the material are MX. This figure is from reference (Zhang, Sham, and Li 2021).

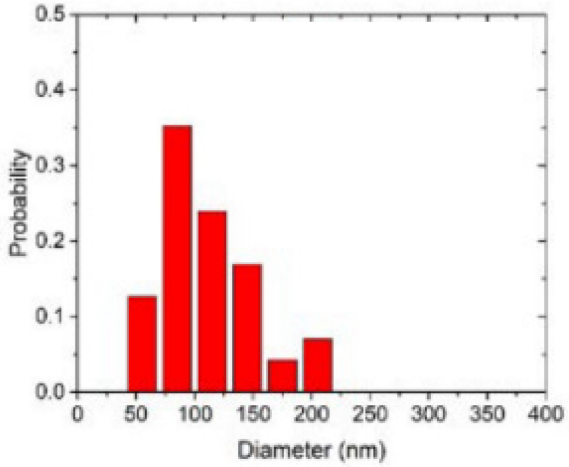

Figure 2. MX precipitate size distribution for Commercial Heat 1 – SA. This figure is from reference (Zhang, Sham, and Li 2021).

2.2.2 Commercial Heat 1 – PT

Commercial Heat 1 – PT was characterized using TEM. A BF TEM image of the microstructure is shown in Figure 3. Commercial Heat 1 – PT is comprised of precipitates present at the grain boundaries, twin boundaries, and grain interiors (Zhang, Sham, and Li 2021; Song, Clement, and McMurtrey 2021). The remaining paragraphs in this section describe the precipitate(s) present at each location.

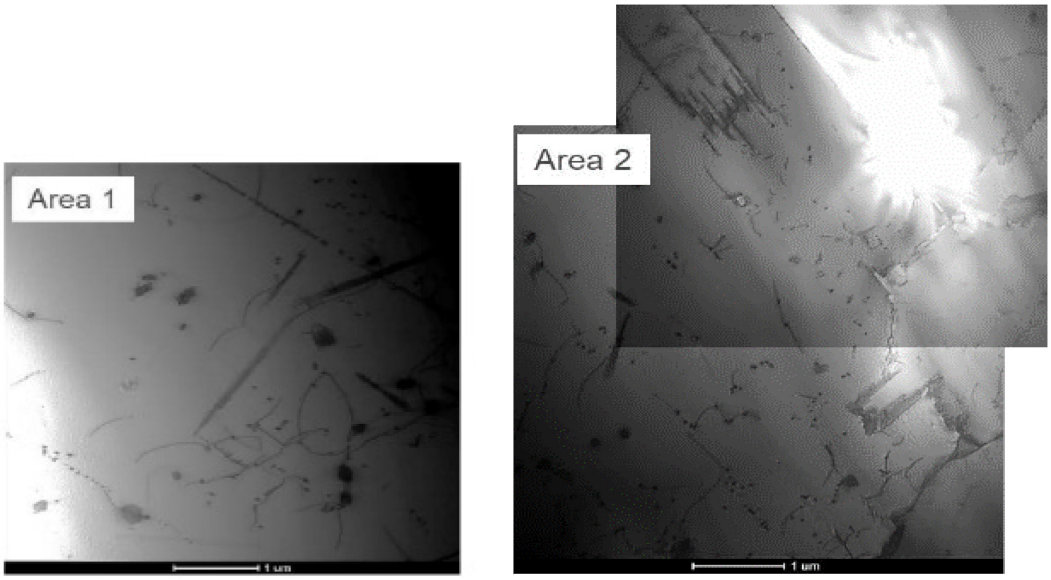

Figure 3. TEM-BF image showing the microstructure of Commercial Heat 1 – PT at low magnification. This figure is from reference (Zhang, Sham, and Li 2021).

Grain boundaries were observed to be decorated with globular Cr- and Mo-rich $M_{23}C_6$ precipitates and MX (Zhang, Sham, and Li 2021; Song, Clement, and McMurtrey 2021). The formation of globular $M_{23}C_6$ precipitates at a grain boundary is shown in Figure 4. These precipitates were 154 µm plus or minus 28 µm with the chemical composition shown in Table 2 (Song, Clement, and McMurtrey 2021). The MX precipitates at the grain boundary were 218 µm plus or minus 34 µm. They were only reported by Song (Song, Clement, and McMurtrey 2021).

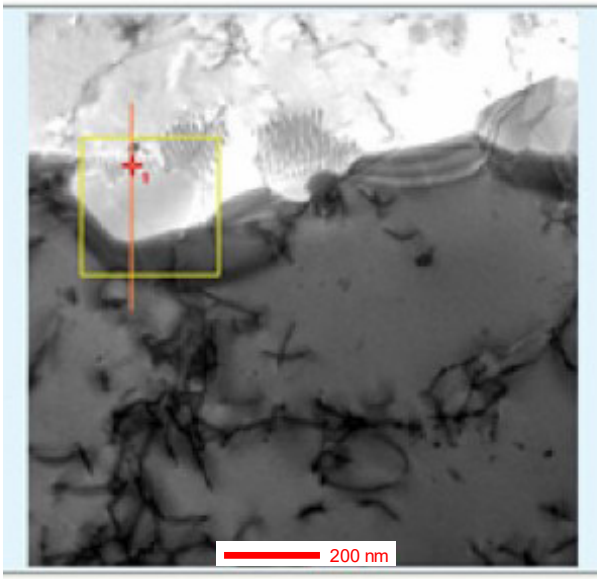

Figure 4. Scanning Transmission Electron Microscopy (STEM) image of Cr- and Mo-rich $M_{23}C_6$ precipitates forming at grain boundaries. This figure is modified from reference (Song, Clement, and McMurtrey 2021).

Table 2. Chemical composition (in at. %) of the globular $M_{23}C_6$ precipitates observed at the grain boundaries and within the grain interiors in Commercial Heat 1 – PT (Song, Clement, and McMurtrey 2021).

C(K)	Cr(K)	Fe(K)	Ni(K)	Mo(K)
6.57 ± 2.31	37.00 ± 4.91	37.49 ± 4.61	15.67 ± 2.67	1.45 ± 0.33

Twin boundaries were observed to be decorated with Cr- and Mo-rich $M_{23}C_6$ precipitates. These $M_{23}C_6$ precipitates at an incoherent twin boundary are shown in Figure 5. The sample shown in Figure 5 is from Commercial Heat 1, but it was heat treated at 775°C for 10 hours followed by a water quench instead of the standard air cool (Song, Clement, and McMurtrey 2021). As mentioned in Section 2.1, the precipitates are not expected to be significantly impacted by whether the precipitation treatment was subsequently air cooled or water quenched. Consequently, these $M_{23}C_6$ precipitates are expected to be present in Commercial Heat 1 – PT with air cooling. This expectation is substantiated in the top left-hand corner of Area 2 in Figure 3 which shows $M_{23}C_6$ precipitates on an incoherent twin boundary in Commercial Heat 1. These $M_{23}C_6$ precipitates on the incoherent twin boundaries are 201 µm plus or minus 58 µm in length and 48 µm plus or minus 6 µm in width. On the coherent twin boundaries, the $M_{23}C_6$ precipitates are 288 µm plus or minus 48 µm long and 26 µm plus or minus 4 µm wide. The chemical composition of these $M_{23}C_6$ precipitates is shown in Table 3 (Song, Clement, and McMurtrey 2021).

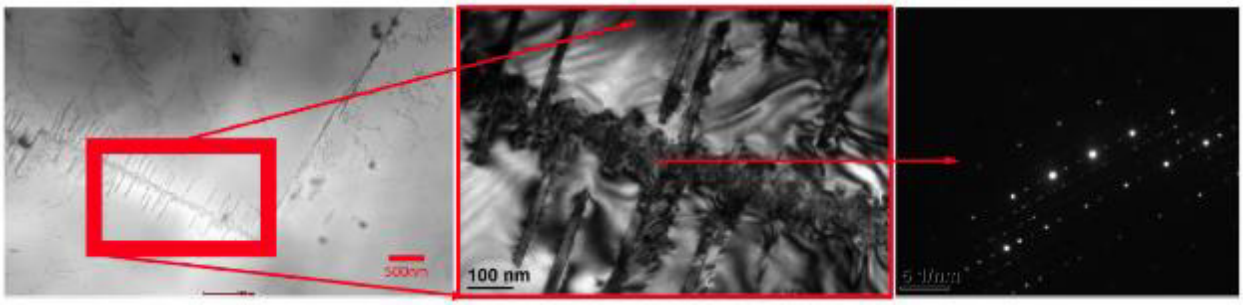

Figure 5. TEM-BF images (left and middle) with diffraction pattern (right) showing $M_{23}C_6$ precipitates on an incoherent twin boundary in Commercial Heat 1 that was heat treated at 775°C for 10 hours followed by a water quench. This figure is from reference (Song, Clement, and McMurtrey 2021).

Table 3. Chemical composition (in at. %) of the $M_{23}C_6$ precipitates on incoherent twin boundaries in Commercial Heat 1 – PT (Song, Clement, and McMurtrey 2021).

C(K)	Cr(K)	Fe(K)	Ni(K)	Mo(K)
12.92 ± 0.75	46.36 ± 0.98	24.55 ± 0.89	9.63 ± 0.49	2.29 ± 0.12

Within the grain interiors the following precipitates were observed: (a) MX core with $M_{23}C_6$ shell; (b) spherical MX; (c) Nb-rich MX or Z-phase (CrNbN) that is less than 10 nm in diameter; (d) globular $M_{23}C_6$; and (e) chain-like $M_{23}C_6$. The MX core with $M_{23}C_6$ shell precipitate is shown in Figure 6 (Song, Clement, and McMurtrey 2021). A spherical MX precipitate with an energy dispersive spectroscopy (EDS) line scan is shown in Figure 7. These precipitates are 185 μm plus or minus 21 μm in size with the chemical composition provided in Table 4. The nanosized Nb-rich precipitates appear to preferentially form on dislocations. Their small size makes it challenging to identify these precipitates as either MX or Z-phase. EDS maps are usually inconclusive, owing to thickness effects of the TEM foils and clean diffraction patterns that can be difficult to get. Figure 8 shows some of these precipitates in the microstructure, including some of the larger 200 nm sized Nb-rich precipitates as well as nanoscale Nb-rich precipitates on dislocations. Figure 9 shows the nanosized dislocations at a higher magnification. Table 4 gives the composition and size distribution of MX precipitates (Song, Clement, and McMurtrey 2021). The globular $M_{23}C_6$, only reported by Song, was found to be 168 μm plus or minus 21 μm. It was only reported by Song (Song, Clement, and McMurtrey 2021). Chain-like $M_{23}C_6$ was observed that could extend microns in length. Figure 8 shows two instances of chain-like $M_{23}C_6$. Sometimes these precipitate

chains nucleated on the MX core with $M_{23}C_6$ shell precipitate (Zhang, Sham, and Li 2021; Song, Clement, and McMurtrey 2021).

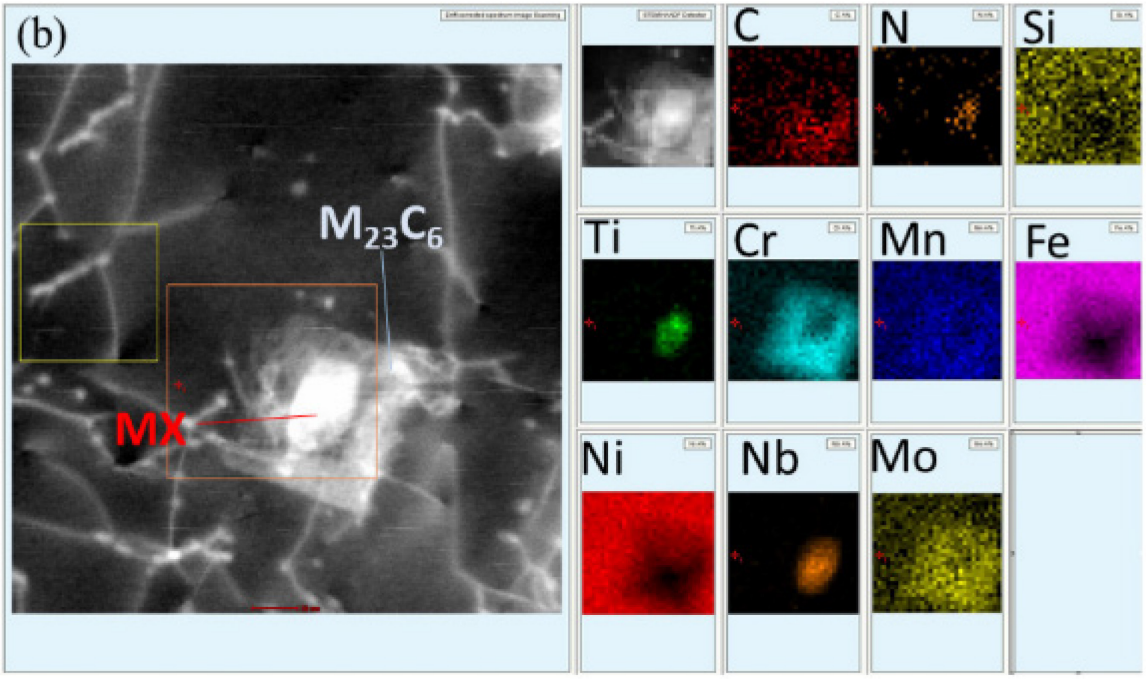

Figure 6. STEM image with EDS map showing MX core with $M_{23}C_6$ shell precipitate seen in Commercial Heat 1 – PT. This figure is from reference (Song, Clement, and McMurtrey 2021).

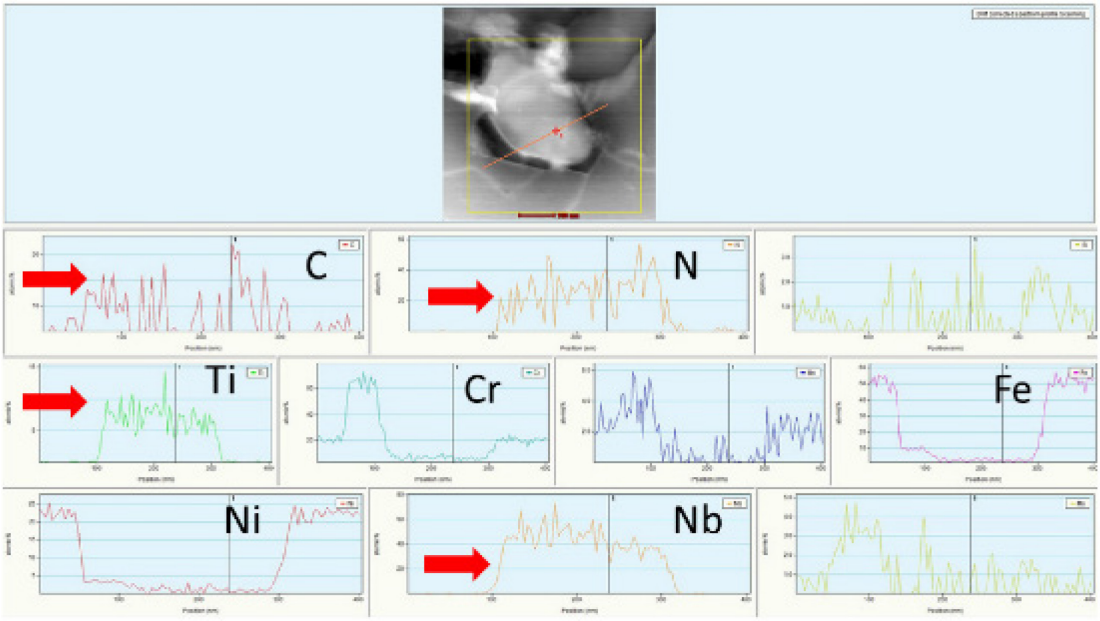

Figure 7. STEM image with EDS line scan showing spherical MX precipitate seen in Commercial Heat 1 – PT. This figure is from reference (Song, Clement, and McMurtrey 2021).

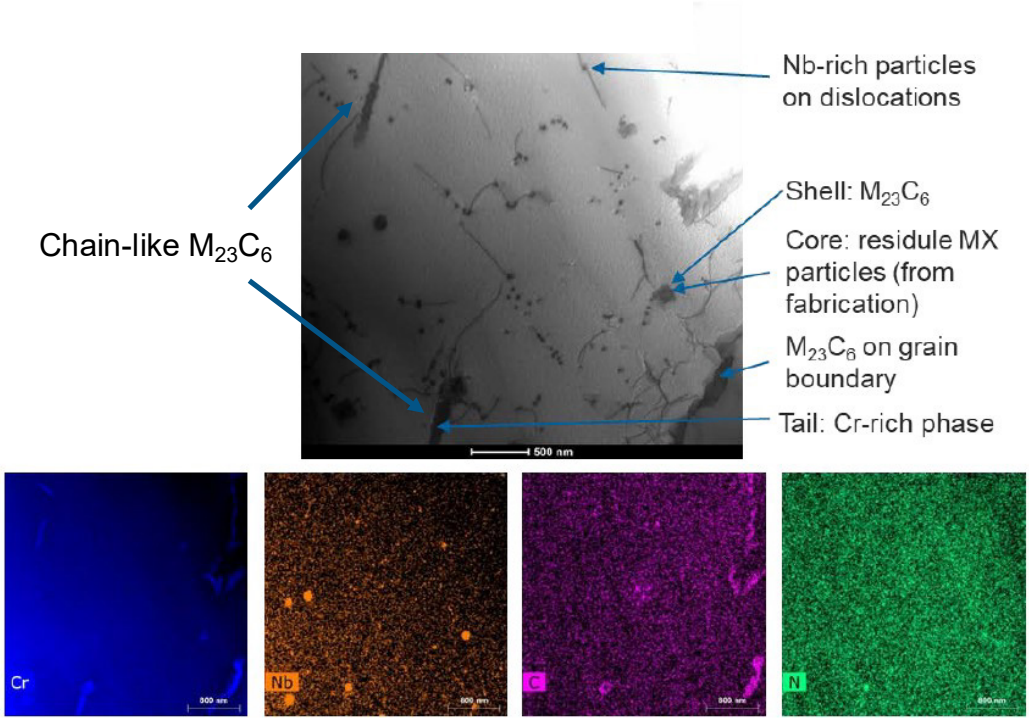

Figure 8. STEM image with EDS map showing precipitates in Commercial Heat 1 – PT with EDS map. This figure has been modified from reference (Zhang and Sham 2020).

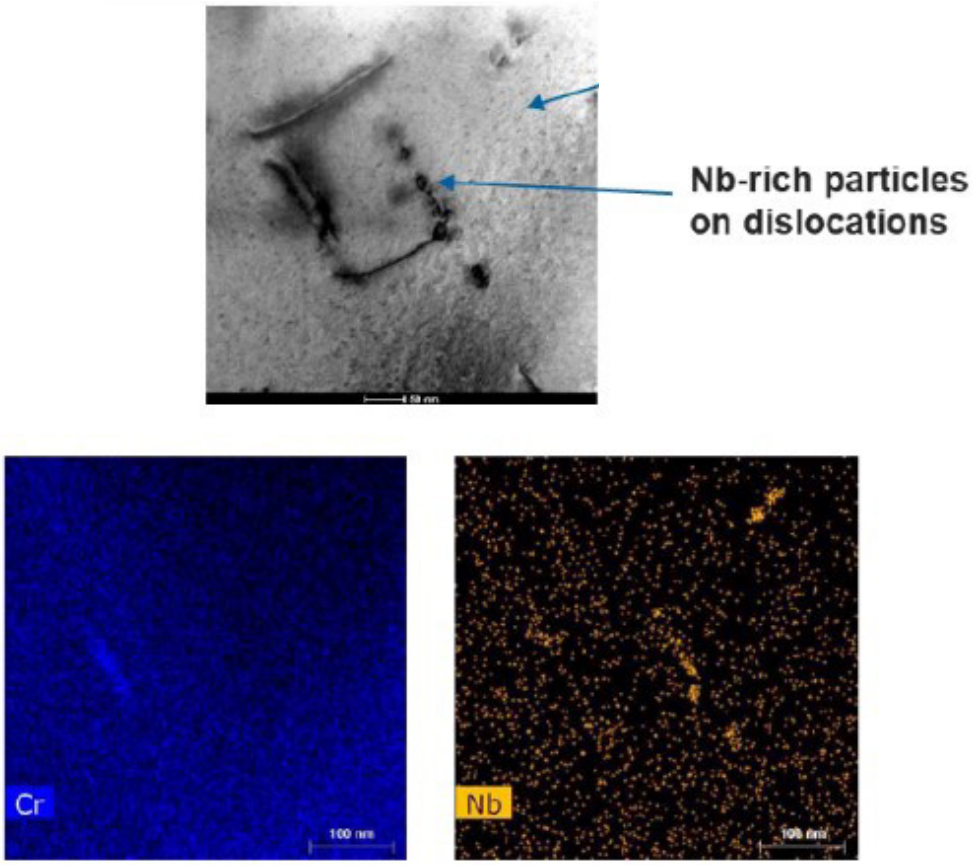

Figure 9. High-magnification STEM image and EDS map showing nanosized precipitates on dislocations in Commercial Heat 1 – PT. This figure is modified from reference (Zhang and Sham 2020).

Table 4. Chemical composition (in at. %) of the MX precipitates in Commercial Heat 1 – PT (Song, Clement, and McMurtrey 2021).

C(K)	N(K)	Ti(K)	Fe(K)	Ni(K)	Nb(K)
0.58 ± 0.27	3.43 ± 0.91	3.41 ± 0.91	33.21 ± 2.86	15.20 ± 1.4	23.49 ± 3.78

3. PURPOSE

The FY 2022 work conducted at INL associated with A709 precipitates to support the A709 Code Cases encompasses two broad goals:

- Understand the microstructure of Commercial Heat 2 and determine if the precipitates seen in this heat are comparable with those found in Commercial Heat 1
- Understand the impact of variations in the time and temperature of the precipitation treatment for A709.

Developing an understanding of the precipitates present in Commercial Heat 2 in both the SA and PT conditions is critical to understanding its mechanical properties. Differences in the mechanical properties between Commercial Heats 1 and 2 are likely correlated with differences in the precipitates between the two heats. Consequently, TEM was utilized to characterize the precipitates found in Commercial Heat 2, both in the SA condition and PT condition. The following direct comparisons were made:

- Commercial Heat 1 – SA vs. Commercial Heat 2 – SA
- Commercial Heat 1 – PT vs. Commercial Heat 2 – PT
- Commercial Heat 2 – SA vs. Commercial Heat 2 – PT.

Precipitation treatment of Commercial Heat 1 resulted in the precipitation of the beneficial MX and Z-phase and was observed to improve creep-fatigue properties without significantly impacting creep properties (Rupp and McMurtrey 2020). The implementation of the precipitation treatment on an actual component in an industry setting will likely be less controlled. Components used in real world applications might see an undershoot or overshoot from desired precipitation treatment conditions based on the thickness, size, and profile of the component. It is also possible that for larger components, it might be difficult to have uniform temperature throughout the component during precipitation treatment. This may result in an undershoot or overshoot from the desired precipitation treatment for portions of the component. Therefore, it is important to understand the impact of variations in the time and temperature of the precipitation treatment on the properties of A709. Additionally, this information is necessary for justifying the permissible temperature and time ranges for acceptance of the precipitation treatment.

4. EXPERIMENTAL METHODOLOGY

4.1 Precipitate Characterization

4.1.1 Material

Plate CG05455 from Commercial Heat 2 was used for TEM characterization. The plate is nominally 1.806 in. thick with the chemistry shown in Table 5. Samples were taken at approximately one-half the plate length (parallel to the rolling direction), one-half the plate width, and one-quarter the plate thickness. Mechanical test specimens to generate the A709 Code Case data packages were machined from this plate. The radial direction of these specimens was centered at one-quarter the plate thickness in accordance with ASTM standard E8, "Standard Test Methods for Tension Testing of Metallic Materials" (ASTM 2021d). Both the SA and PT conditions were characterized. The precipitation treatment was conducted at INL in accordance with PLN-6567, "Precipitation Treatment of Alloy 709" (INL 2022a).

Table 5. Chemical composition (in wt. %) of Commercial Heat 2 Plate CG05455, heat 529900-01.

C	Mn	Si	P	S	Cr	Ni	Mo
0.08	0.9	0.39	0.003	<0.001	19.9	24.6	1.5

N	Nb	Ti	Cu	Co	Al	B	Fe
0.15	0.17	<0.01	0.06	0.02	0.02	0.004	Balance

4.1.2 TEM Characterization

TEM samples were prepared by punching out 3 mm diameter foils from material that was ground down to be 100 µm thick. These disks were then twin-jet electropolished with a solution that was 5% perchloric acid and 95% methanol at -25°C and 20 V. A Field Electron and Ion Company Tecnai TF30-FEG STwin TEM operating at 300 kV was utilized for TEM characterization. Images were acquired using BF, dark field (DF), and STEM. Only the features that were representative of the entire sample were studied.

It should be noted that precipitate characterization was established from STEM-EDS spectra. In the absence of complementary electron diffraction data, characterization of the precipitate type is limited to determination that they are either MX or Z-phase precipitates. The purpose of precipitate treating the SA material is to reduce the amount of nitride or carbo-nitride forming elements in solution through precipitation of MX or Z-phase precipitates prior to deformation. This precipitate treatment has been shown to restrict the precipitation of the fine MX or Z-phase precipitates on dislocation substructures during subsequent cyclic testing. The result is that there is less cyclic hardening compared to testing SA material and the cycles to failure in creep-fatigue is significantly increased. For the purpose of this investigation, the degree of precipitate characterization presented in this report is sufficient and differentiation between MX and Z-phase precipitates is not considered to be vital.

4.2 Effect of Variations in the Precipitation Treatment

4.2.1 Material

Plate CG05455 from Commercial Heat 2 in the SA condition was investigated. This plate is nominally 1.806 in. thick with the chemistry shown in Table 5. Samples were taken at approximately one-half the plate length (parallel to the rolling direction). The samples were taken at either approximately one-half the plate width or near the edge of the plate with respect to the plate width. Hardness measurements of the solution-annealed material at these two locations were equivalent. The specimens

were roughly 26.5 mm (rolling direction) x 19.5 mm (long transverse direction) x 46 mm thick (short transverse direction).

Precipitation treatment variations of interest were duplicated using specimens from Commercial Heat 1 in the SA condition. These specimens were taken from Plate 58776-RBC2, which is 1.1 in. thick with the chemistry shown in Table 1. Specimens were roughly 18.5 mm (rolling direction) x 19.5 mm (long transverse direction) x 29.5 mm (short transverse direction).

4.2.2 Heat Treating

Heat treating was conducted in accordance with PLN-6567, "Precipitation Treatment of A709 with Variations in Time and Temperature" (INL 2022b). A total of 25 variations of the precipitation treatment were investigated by independently varying the temperature (750, 760, 775, 790, and 800°C) and time (3, 9, 10, 11, and 30 hours). The specimens were subsequently air cooled after completion of the heat treatment. It should be noted that the 775°C for 10 hours heat treatment followed by air cooling is the standard precipitation treatment. Temperature and time during heat treating were maintained within 2.5°C and 10 minutes, respectively, of the prescribed value. For each heat treatment, the temperature was recorded in 10 second intervals.

4.2.3 Hardness Measurements

A LECO LM-310AT hardness tester was used to measure Vickers hardness of the heat treated samples in accordance with PLN-6649, "Hardness Testing" (INL 2022c) as well as ASTM E92-17, "Standard Test Methods for Vickers Hardness and Knoop Hardness of Metallic Materials" (ASTM 2017a) and ASTM E384-17, "Standard Test Method for Microindentation Hardness of Materials" (ASTM 2017b). A 300 gf indention test force and 13-second dwell was used. Samples were polished down a to 3 μm grit. A total of 10 hardness values were measured for each sample; five were taken along the rolling direction at one-half the plate thickness (short transverse) and the other five were taken along the rolling direction at one-quarter the plate thickness (short transverse direction). Care was taken to avoid edges and damaged areas. Statistical significance was ascertained by calculating mean and standard deviation for each sample.

A LECO LM247AT hardness tester was used to measure the Vickers hardness measurements of the Commercial Heat 2 – SA sample. These hardness measurements were in accordance with ASTM standards E92-17 and E384-17 (ASTM 2017a; ASTM 2017b). A 300 gf indention test force with a 13-second dwell time was used. It should be noted that hardness measurements with this hardness tester fell outside the scope of PLN-6649. However, there is no reason to believe that these hardness measurements are not comparable to those measured using the LECO LM-310AT. For this study, the average of 12 hardness measurements were used: six measurements along the rolling direction at one-half the plate thickness (short transverse direction) and six measurements along the rolling direction at one-quarter the plate thickness (short transverse direction).

5. RESULTS

5.1 Precipitate Characterization

5.1.1 TEM – Commercial Heat 2 – SA

In Commercial Heat 2 – SA, precipitates were observed at and near grain boundaries. Grain interiors were typically free of precipitates or dislocations although some were observed. The $M_{23}C_6$ precipitate was the most commonly observed precipitate in this material condition. Each location will be discussed in more detail in the following paragraphs.

At and near the grain boundaries, the following was observed: (a) precipitates that were roughly 1.5 μm in diameter; (b) $M_{23}C_6$ precipitates; (c) Nb-rich precipitates; and (d) MX precipitates. Each of the precipitates will now be discussed. The roughly 1.5 μm in diameter precipitates are shown in Figure 10 and are indicated with the red arrows. EDS point spectra of these precipitates was inconclusive as shown in Figure 11. $M_{23}C_6$ precipitates were commonly seen forming on grain boundaries. Figure 12 shows EDS point spectra of these $M_{23}C_6$ precipitates on a grain boundary. Note that while EDS point spectra for point 1 shows strong Cr peak as well as presence of Mo which identifies $M_{23}C_6$, scan for point 2 does not show the same peaks. While further investigation is needed for this, other point scans in this region confirm $M_{23}C_6$ with strong Cr peaks. One possibility for low-Cr peak for point 2 could be that most of the $M_{23}C_6$ precipitate might be etched away resulting in thin precipitate which then provides a weak signal-to-noise ratio for $M_{23}C_6$. Some Nb-rich precipitates that are either MX or Z-phase were also seen forming on grain boundaries as shown in Figure 13. Literature indicates that $M_{23}C_6$ precipitates may form at the expense of these Nb-rich precipitates (Ding et al 2019). MX precipitates were seen forming near grain boundaries as shown in Figure 14. For the four point scans, point 1 shows strong Nb peaks, whereas point 3 shows strong Ti peaks. Note that while point 2 does not display these strong Nb, Ti, or Mo peaks, this precipitate appears to be smaller in size and is probably superficial in the matrix. This may have caused noise from the matrix to permeate the EDS point scan. Also, the EDS point spectra which indicates the presence of Ti rules out Z-phase with its CrNbN composition. Typically, MX and Z-phase precipitates are challenging to distinguish between. However, because of the large size of these precipitates, EDS point spectra of these precipitates has a better signal-to-noise ratio, permitting MX and Z-phase precipitates to be distinguished.

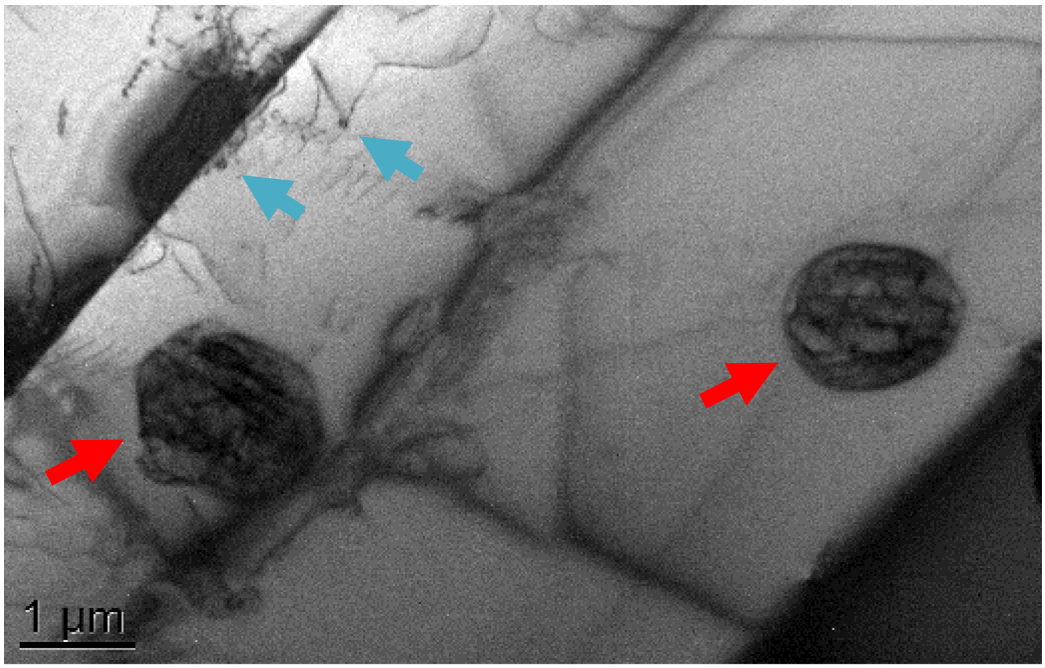

Figure 10. TEM-BF image showing precipitates that are roughly 1.5 µm in diameter, indicated with the red arrows, as well as nanoscale precipitates on dislocations near a twin boundary, indicated by the blue arrows, in Commercial Heat 2 – PT.

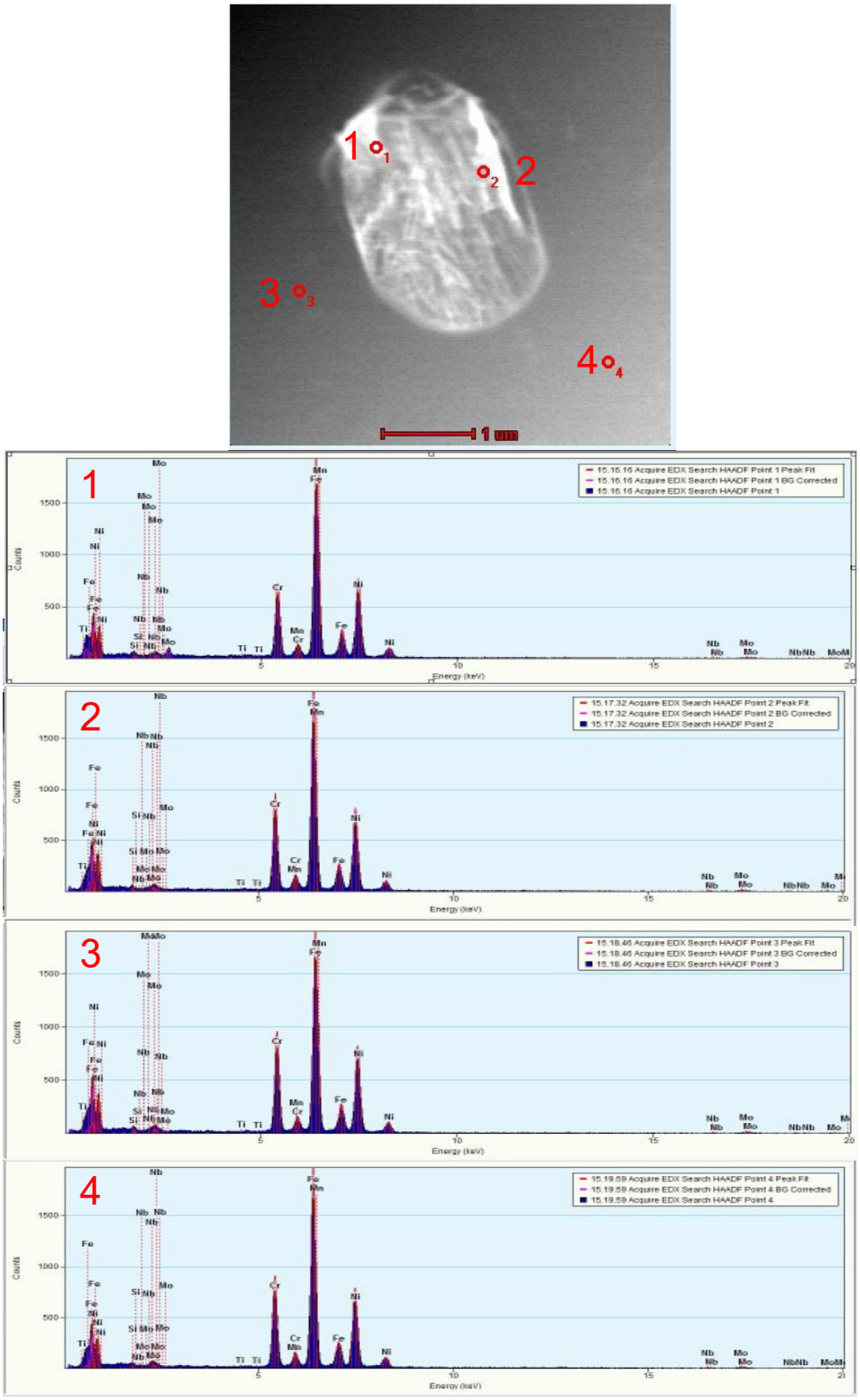

Figure 11. STEM image of a precipitate that is roughly 1.5 µm in diameter. EDS point spectra of the precipitate (Points 1 and 2) as well as the surrounding matrix (Points 3 and 4). Slight variations in the Cr content were observed between the precipitate and the surrounding matrix. EDS inconclusive.

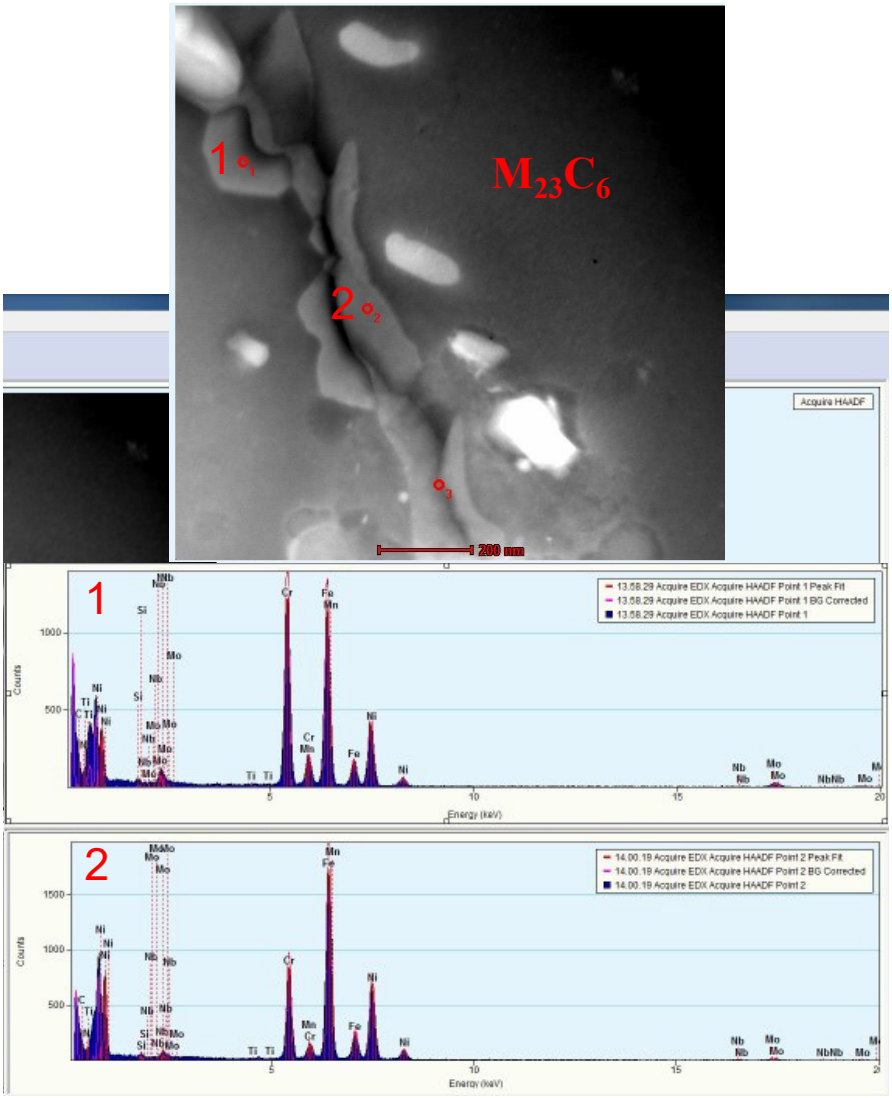

Figure 12. STEM image with EDS point spectra showing $M_{23}C_6$ precipitates on grain boundary (Points 1 and 2).

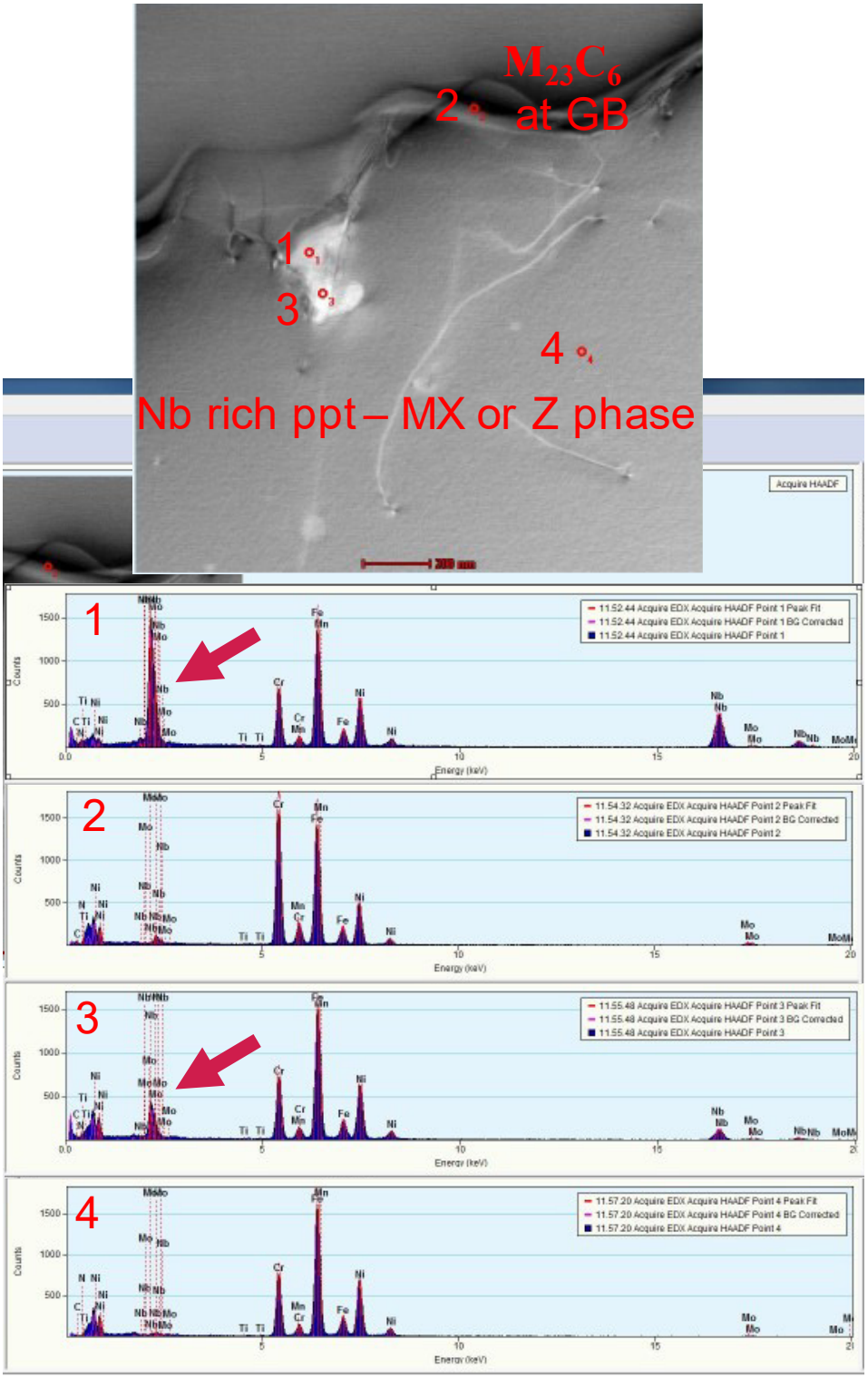

Figure 13. STEM image showing larger Nb-rich precipitates on grain boundary. EDS point spectra of the Nb-rich precipitate (Points 1 and 3), $M_{23}C_6$ precipitate at a grain boundary (Point 2), and surrounding matrix (Point 4). The red arrow in the EDS point spectra for points 1 and 3 highlight the strong Nb peaks.

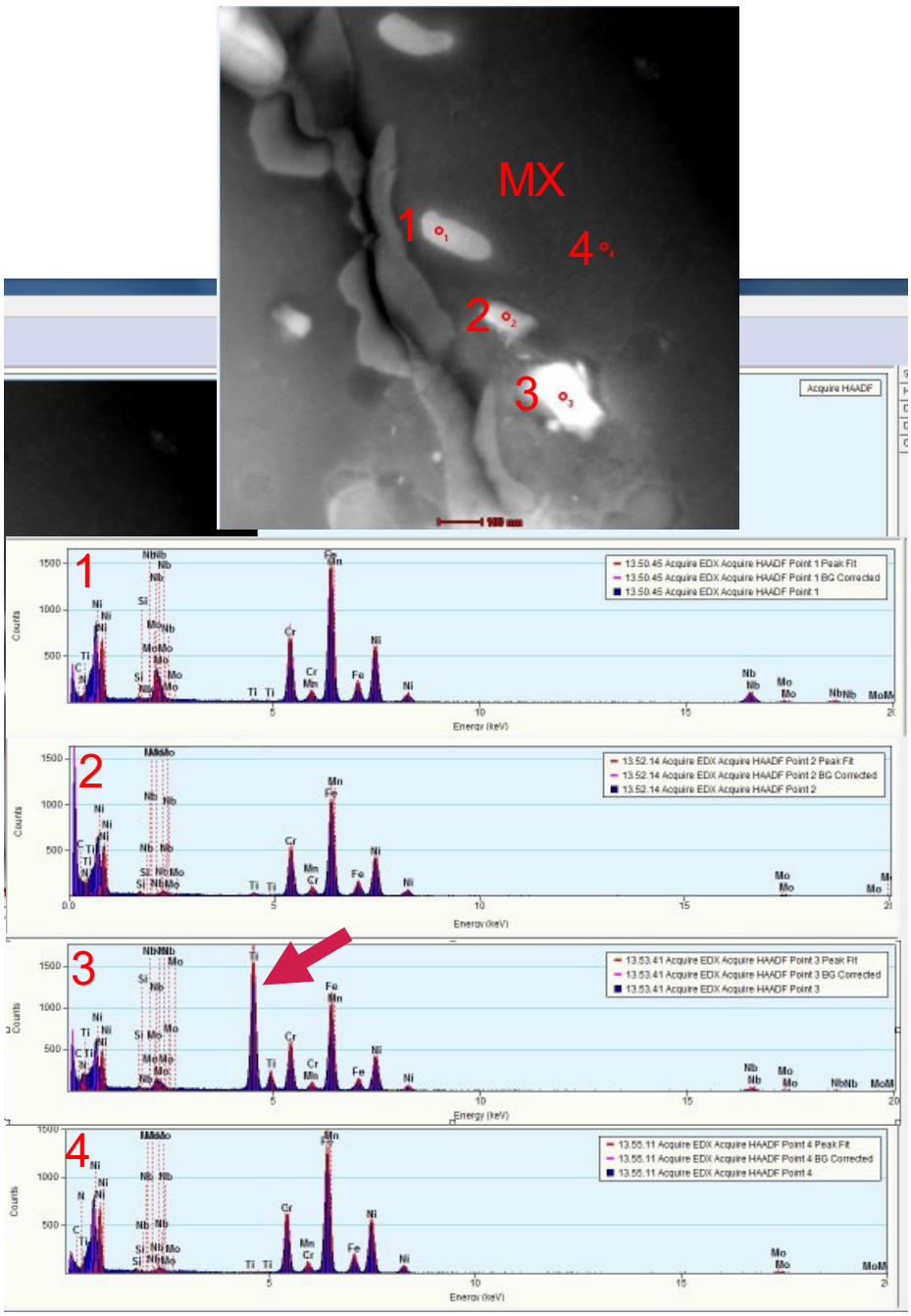

Figure 14. STEM image and EDS point spectra of the Ti-rich MX precipitates near a grain boundary (Points 1, 2 and 3) and surrounding matrix (Point 4). The red arrow in EDS point spectra for point 3 highlights the strong Ti peak.

Typically, the grain interiors were free of precipitates and dislocations as seen in Figure 15. The small number of dislocations that were observed were typically restricted to local clusters. A dislocation-free microstructure is expected from a material condition that has not been subjected to mechanical testing. Nb-rich precipitates that were roughly 30 nm in diameter were also observed in the grain interiors. These precipitates are shown in Figure 16 and also indicated with the blue arrows in Figure 10. These precipitates were usually found nucleating on or pinning dislocations, but free-floating nanosized particles were also observed. As mentioned earlier, characterization of these precipitates is limited to indicating

that they are either MX or Z-phase, and further differentiation between the two is not considered vital for the scope of this study.

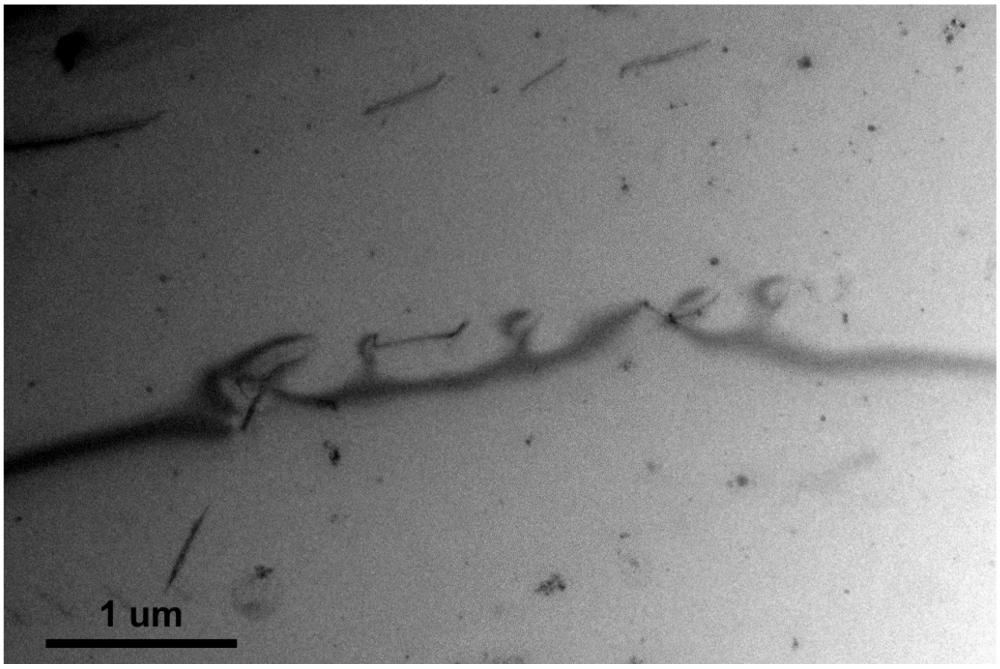

Figure 15. TEM-BF image showing the typical grain interior in Commercial Heat 2 – SA which is free of precipitates and dislocations.

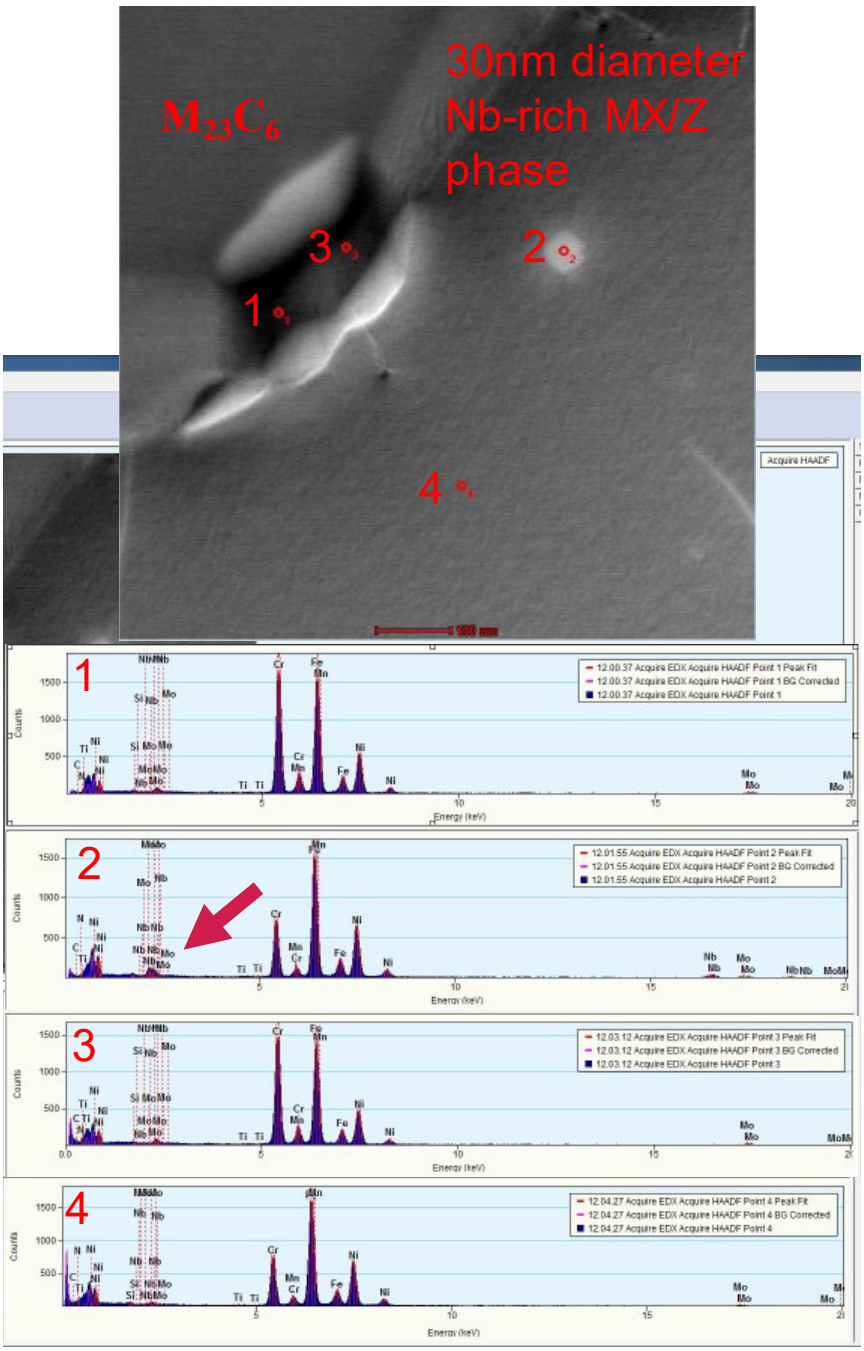

Figure 16. STEM image and EDS spectra showing a Nb-rich precipitate that is roughly 30 nm in diameter near a grain boundary (Point 2), $M_{23}C_6$ at a grain boundary (Points 1 and 3), and the surrounding matrix (Point 4). The arrow in the EDS point spectra for point 2 highlights the Nb peak.

5.1.2 TEM – Commercial Heat 2 – PT

In Commercial Heat 2 – PT, precipitates were seen at the grain boundaries. Precipitates and dislocations were observed within the grain interiors. $M_{23}C_6$ was the most commonly observed precipitate in this material condition. Each location will be discussed in more detail in the following paragraphs.

At and near the grain boundaries the following was observed: (a) $M_{23}C_6$ precipitates; (b) MX core with $M_{23}C_6$ shell precipitates; and (c) MX precipitates. An example of the $M_{23}C_6$ precipitates is shown in

Figure 17 as indicated by the red arrows. EDS point spectra of the $M_{23}C_6$ precipitates are shown in Figure 18 and Figure 19 as indicated by the high-intensity Cr peaks. In Figure 18, the signal-to-noise ratio for EDS point spectra for points 1 and 2 is particularly high because these precipitates are protruding into the hole of the TEM foil. An example of a MX core with $M_{23}C_6$ shell precipitate at a grain boundary is shown in Figure 19 and Figure 20. Point 2 in Figure 19 is the same precipitate shown in Figure 20. The high Cr peak and high Nb peak observed for point 1 in Figure 19 indicates that this is also a MX core with $M_{23}C_6$ shell precipitate. The following should be noted from the EDS line scan in Figure 20: (a) the narrow Nb and Ti peaks marked with the red arrows that correlate to the MX core; (b) the broad Cr peak indicating the $M_{23}C_6$ shell; and (c) the decrease in Fe and Ni within the precipitate but present in the matrix. Some MX precipitates were observed around the grain boundary as shown in Figure 17 and Figure 19. MX precipitates near grain boundary are highlighted in orange in Figure 17.

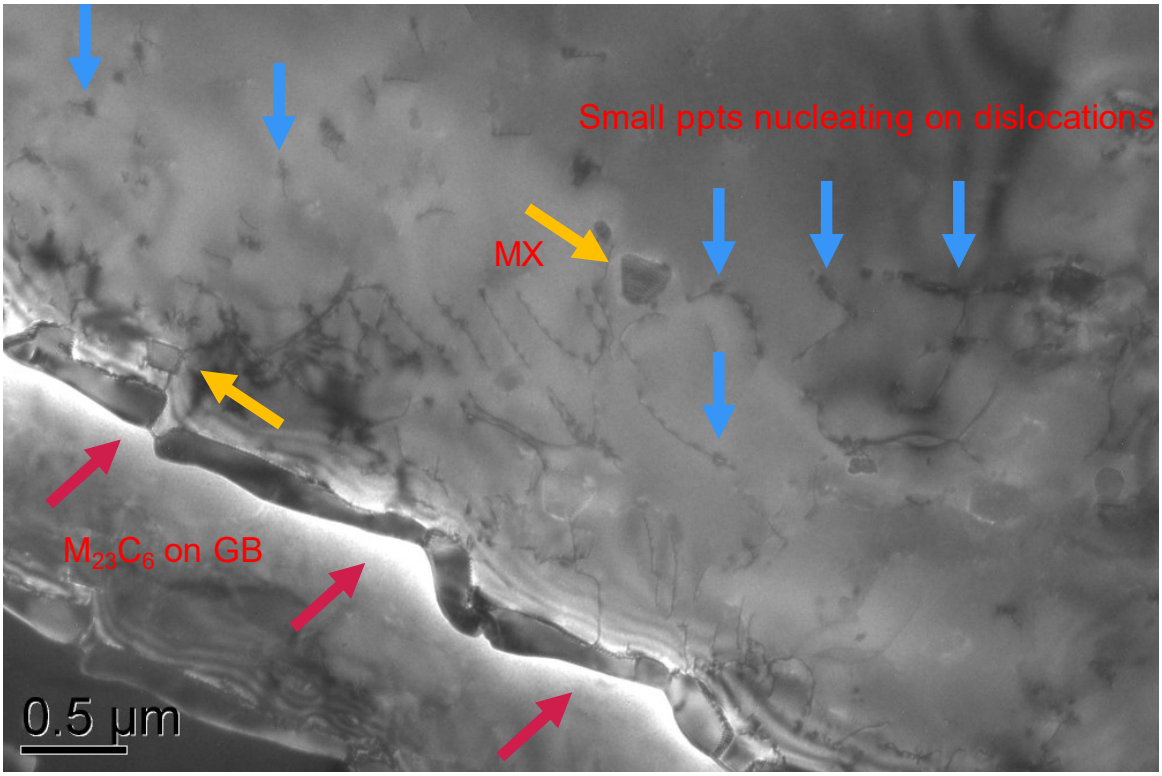

Figure 17. TEM-BF image showing $M_{23}C_6$ precipitate on grain boundaries (red arrows), MX near grain boundaries (yellow arrows), and small precipitates nucleating on dislocations (blue arrows).

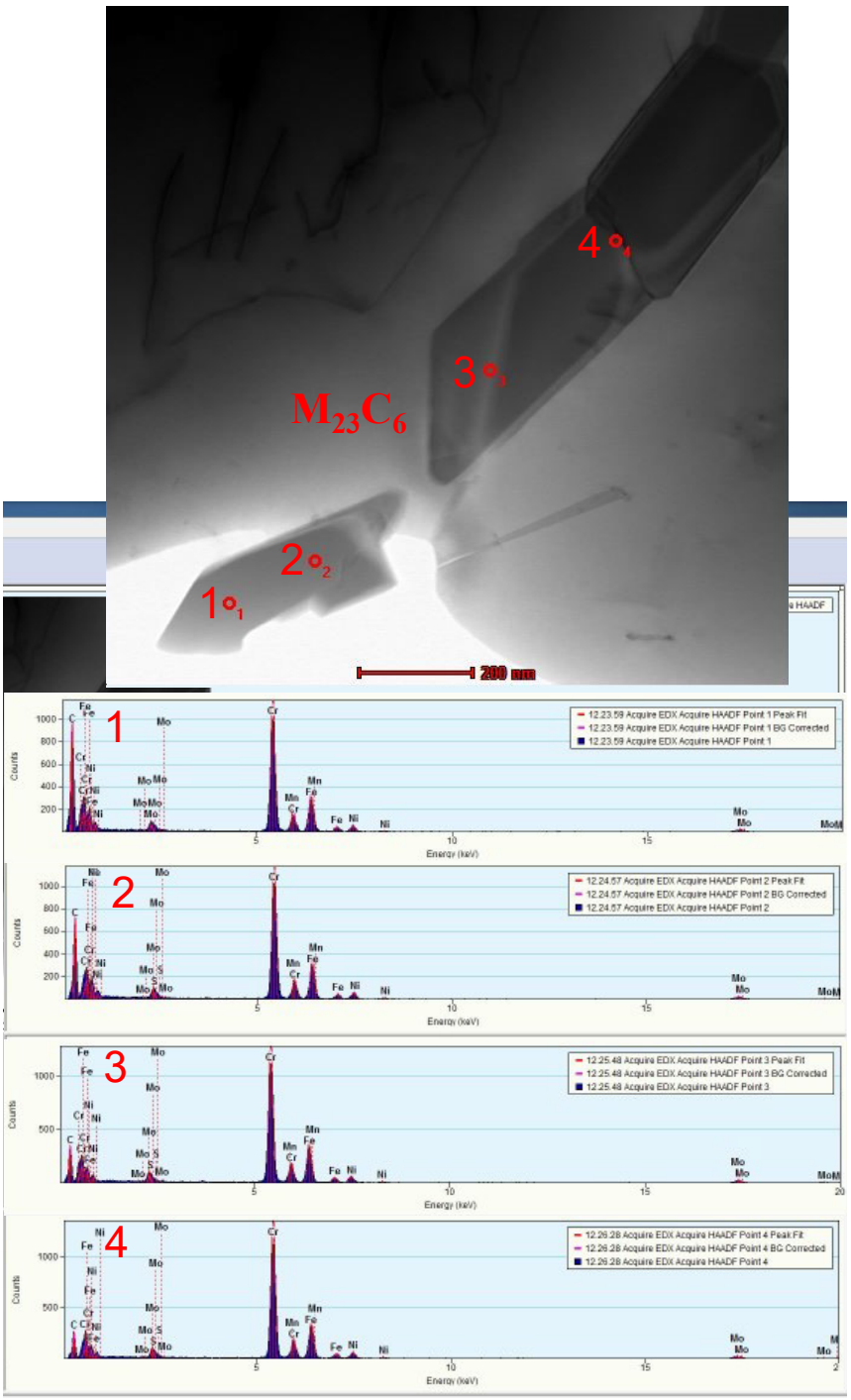

Figure 18. STEM image with EDS point spectra showing $M_{23}C_6$ precipitate on grain boundary (points 1 through 4).

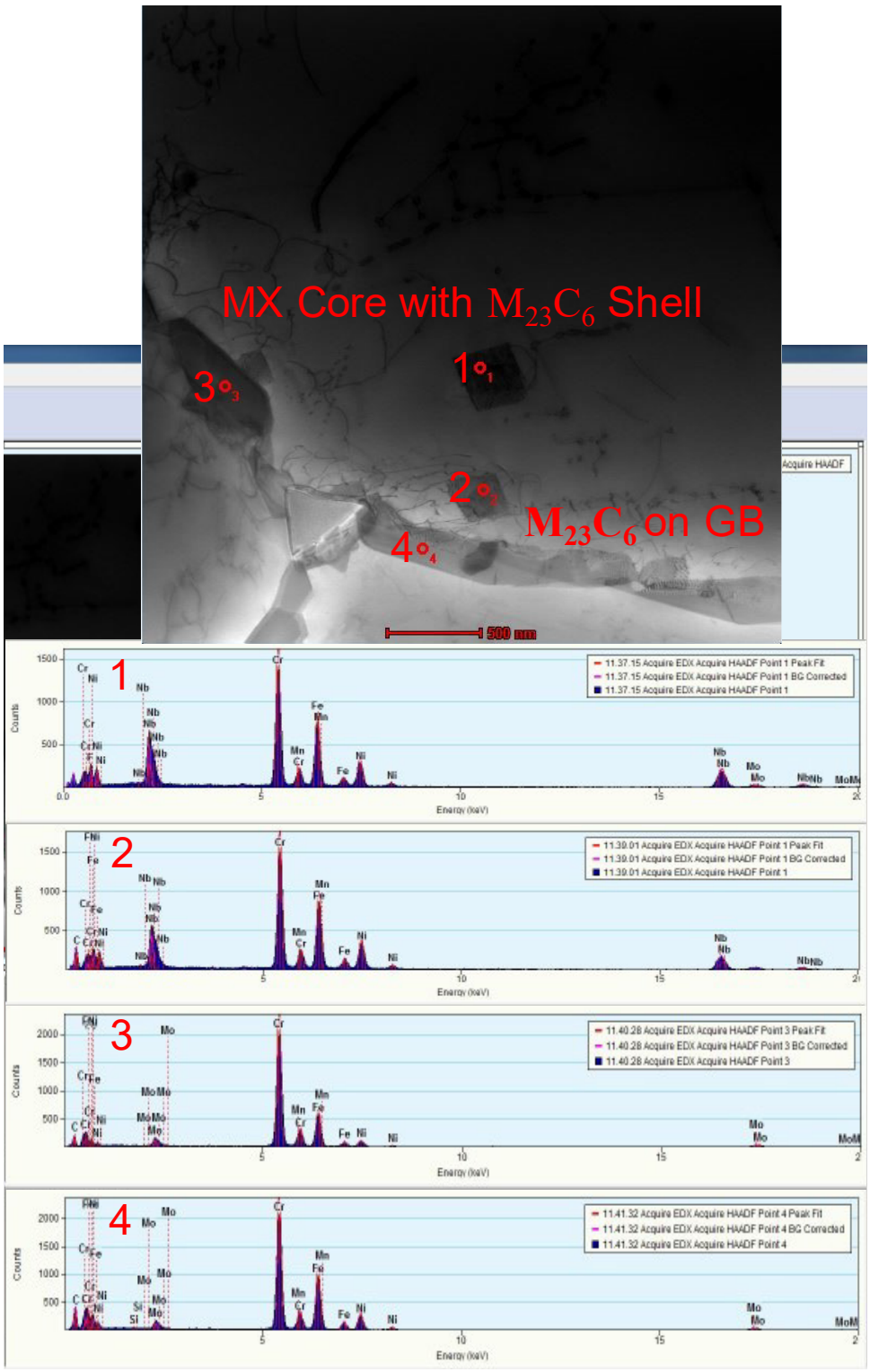

Figure 19. STEM image with EDS point spectra of MX core with $M_{23}C_6$ shell precipitate structure near the grain boundaries (Points 1 and 2) and $M_{23}C_6$ precipitate at the grain boundaries (Points 3 and 4).

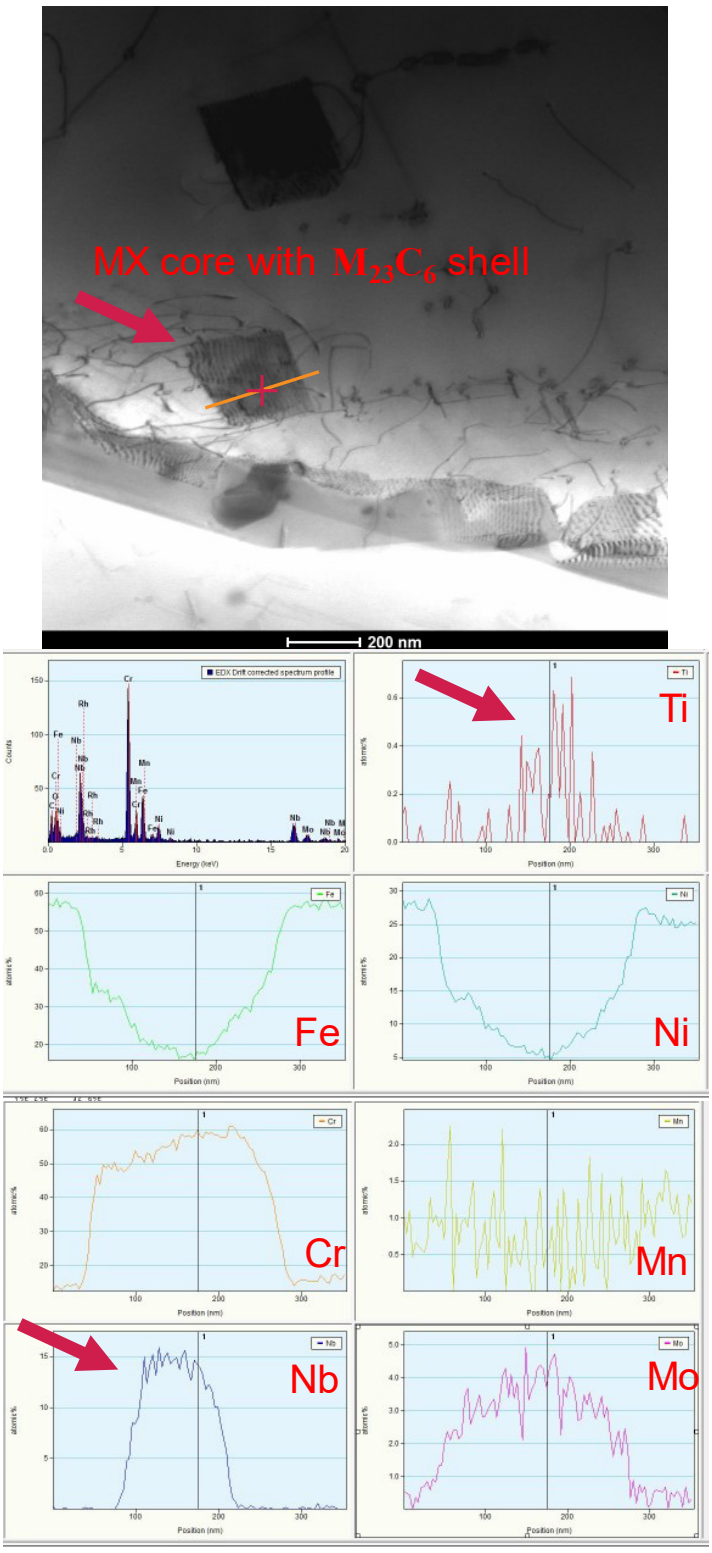

Figure 20. STEM image with EDS line scan of a MX core with $M_{23}C_6$ shell precipitate near a grain boundary.

A BF TEM image of a typical grain interior is shown in Figure 21 which contained dislocations and precipitates. Similar to Commercial Heat 2 – SA, the small number of dislocations that were observed

were typically restricted to local clusters. Unlike Commercial Heat 2 – SA, an increased number of nanosized precipitates were observed to have formed on the dislocations as shown in Figure 22 and by the blue arrows in Figure 17. In Figure 22, it appears that dislocations have been generated by a Frank-Reed source. The high density of nanosized precipitates on these dislocations were not observed to have the same density in the Commercial Heat 2 – SA condition. This indicates that the precipitates nucleated on the dislocations during the precipitation treatment. The alternative would be for the precipitates to have simply pinned these precipitates. Higher magnification images of the nanosized precipitates are shown in Figure 23 and Figure 24. While most of these precipitates nucleate on dislocations, some are seen free-floating in the matrix. In this material condition, two distinct sizes of the nanosized precipitates are observed: some are roughly 65 nm in diameter whereas others are roughly 25 nm in diameter. While EDS was ineffective in determining the composition of these precipitates, work on Commercial Heat 1 – PT at ANL have determined precipitates of similar size to be MX or Z-phase (Zhang et al, 2021). MX core with $M_{23}C_6$ shell precipitates were also observed within the grain interiors as shown in Figure 25 indicated by the strong Nb peaks in the EDS point spectra. A spherical MX precipitate was observed in the grain interior as shown in Figure 25 and labeled 4. This precipitate was not commonly observed in the Commercial Heat 2 – PT microstructure.

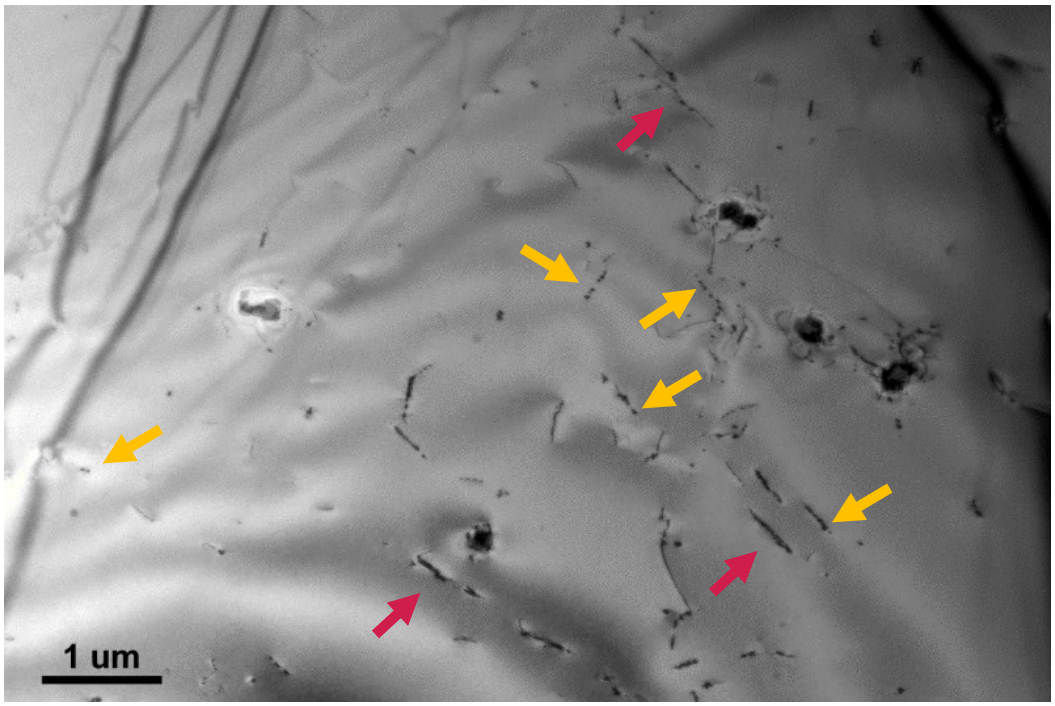

Figure 21. TEM-BF image showing the grain interior. Red arrows show dislocations in the matrix, whereas yellow arrows highlight nanosized precipitates that are free-floating within the matrix and on dislocations.

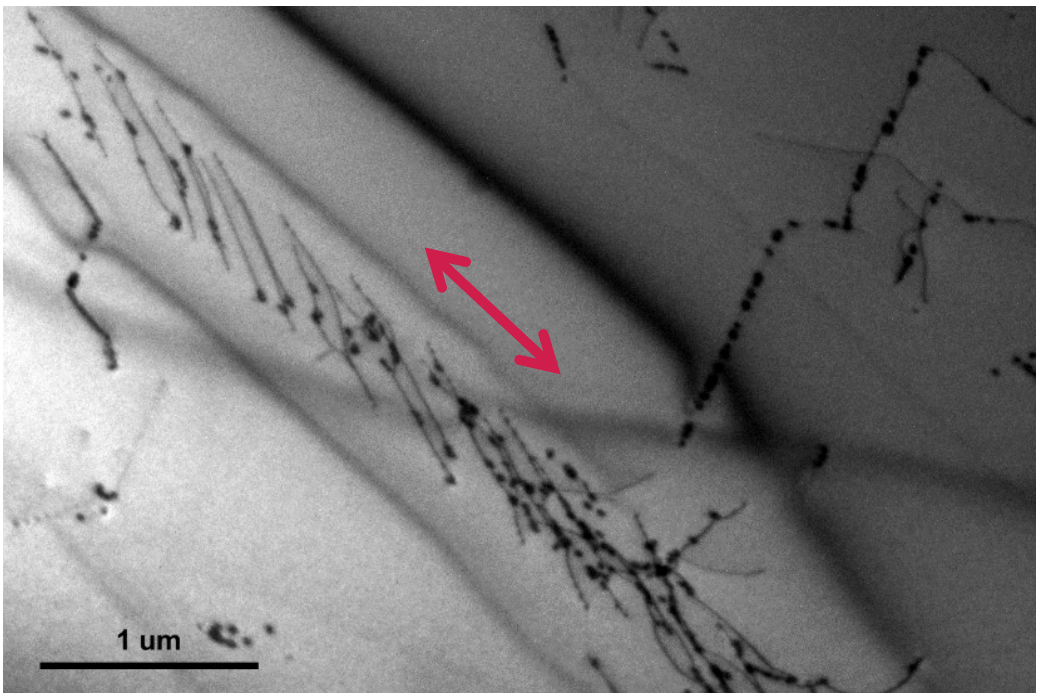

Figure 22. TEM-BF image of the grain interior at a higher magnification showing a high density of nanosized precipitates on the dislocations. Red arrow indicates possible directions of dislocation motion generated from a Frank-Reed source (not in micrograph).

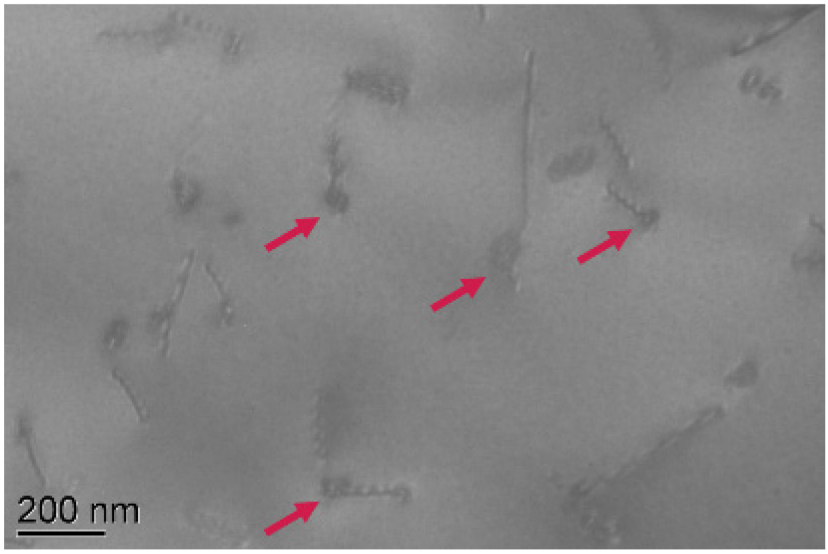

Figure 23. STEM image showing roughly 65 nm precipitates pinning dislocations highlighted by the red arrows.

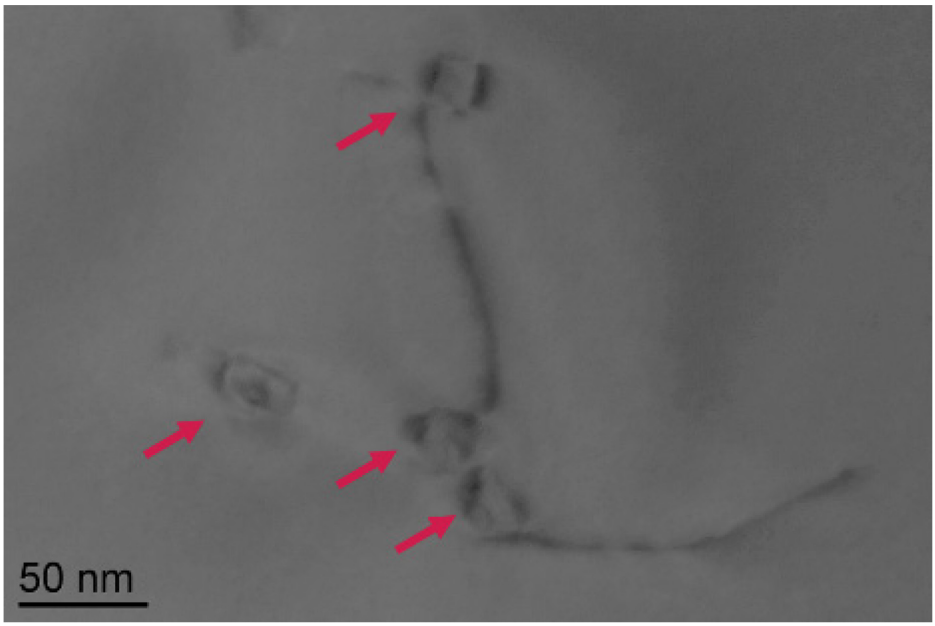

Figure 24. STEM image showing smaller roughly 25 nm precipitates on or near dislocations highlighted by the red arrows.

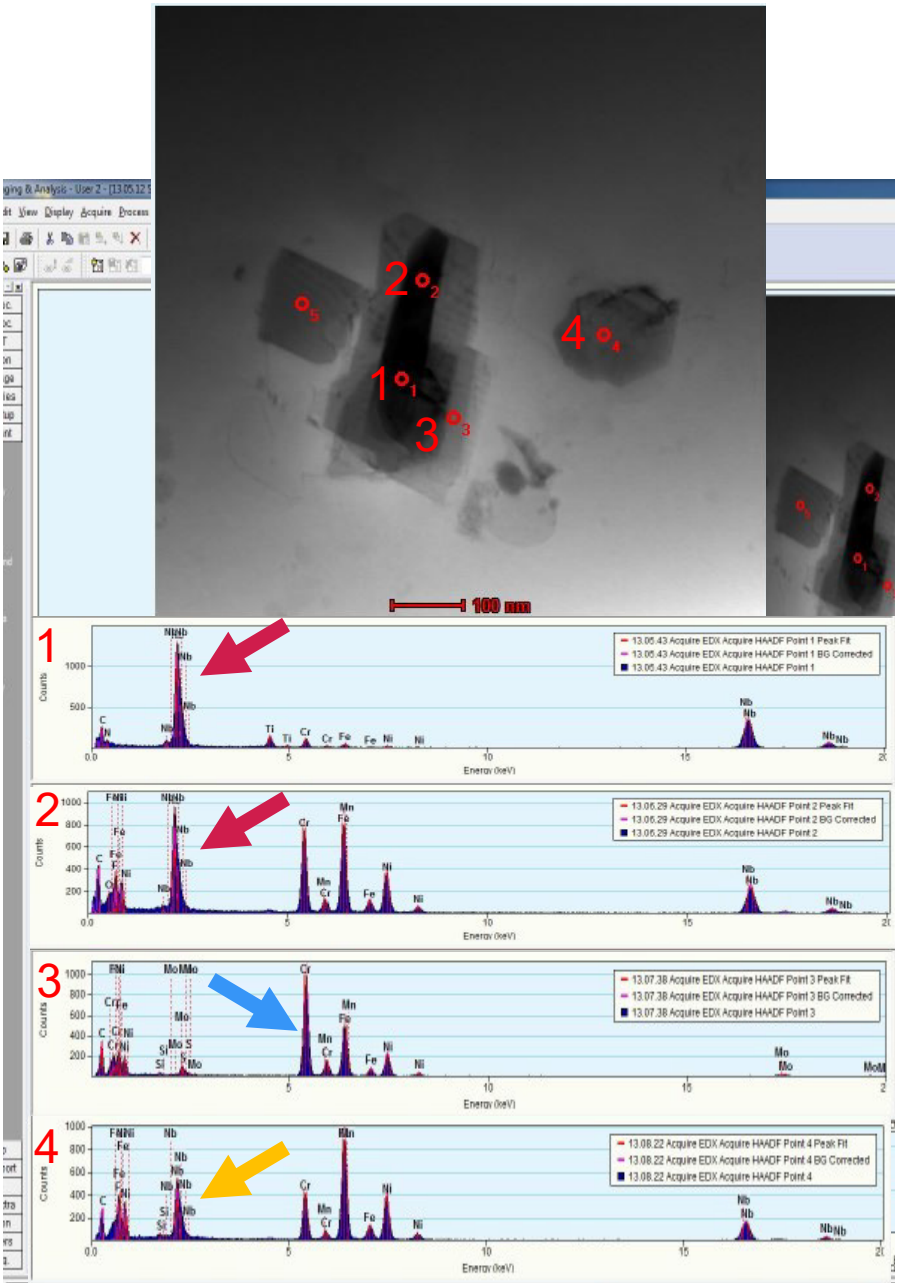

Figure 25. STEM image with EDS point spectra of MX core with $M_{23}C_6$ shell precipitate observed within the grain interior. Red arrows highlight strong Nb peaks on the EDS point spectra for points 1 and 2 indicating MX core, and the blue arrow indicates $M_{23}C_6$ shell with a strong Cr peak for point 3. A MX precipitate is seen in the vicinity with strong Nb peaks, as denoted by the yellow arrow in the EDS point spectra for point 4.

5.1.3 Comparison of Commercial Heat 1 – SA *versus* Commercial Heat 2 – SA

Commercial Heat 2 – SA and Commercial Heat 1 – SA were both observed to contain comparable MX precipitates. $M_{23}C_6$ precipitates on grain boundaries, small Nb-rich MX or Z-phase precipitates within the grain interior, and large 1.5 µm precipitates were only observed to be present in Commercial Heat 2 – SA.

5.1.3 Comparison of Commercial Heat 1 – PT *versus* Commercial Heat 2 – PT

The following was observed in both Commercial Heat 1 – PT and Commercial Heat 2 – PT: (a) $M_{23}C_6$ precipitates at the grain boundaries; (b) MX core with $M_{23}C_6$ shell precipitates within the grain interiors; and (c) nanosized MX or Z-phase precipitates within the grain interiors. It should be noted that only one instance of an incoherent twin boundary, decorated with Cr- and Mo-rich $M_{23}C_6$ precipitates, was observed in Commercial Heat 2 – PT. This precipitate structure was observed in Commercial Heat 1 – PT. The BF TEM images shown in Figure 26 show the $M_{23}C_6$ precipitates on an incoherent twin boundary in both Commercial Heat 1 – PT and Commercial Heat 2 – PT. A notable difference between the two material conditions was that chain-like $M_{23}C_6$ precipitates were seen in Commercial Heat 1 – PT. An example of this precipitate structure is shown in top left corner of Figure 8. These precipitate chains were not observed in Commercial Heat 2 – PT.

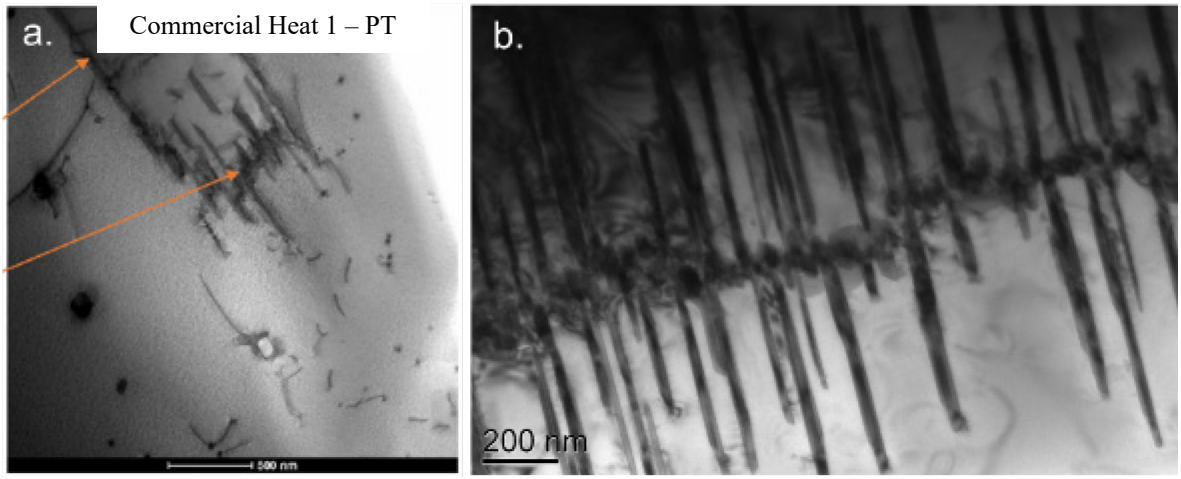

Figure 26. TEM-BF image showing $M_{23}C_6$ precipitates at incoherent twin boundary in Commercial Heat 1 – PT (a) and Commercial Heat 2- PT (b). The precipitate shown in (b) was confirmed to be $M_{23}C_6$ by an EDS line scan.

5.1.3 Comparison of Commercial Heat 2 – SA *versus* Commercial Heat 2 – PT

Both Commercial Heat 2 – SA and Commercial Heat 2 – PT were observed to have $M_{23}C_6$ precipitates and MX precipitates present at the grain boundaries. The density of the MX precipitates remained the same between the two conditions. However, the density of the $M_{23}C_6$ precipitates was significantly higher in Commercial Heat 2- PT. The $M_{23}C_6$ precipitates were observed at the grain boundaries, twin boundaries, and within the grain interior for Commercial Heat 2 – PT. While in Commercial Heat 2 – SA, the $M_{23}C_6$ precipitate is only present at the grain boundaries. Nanosized MX or Z-phase precipitates were seen in both conditions.

5.2 Effects of Variations in the Precipitation Treatment

Figure 27 shows the hardness measured for each Commercial Heat 2 precipitation treatment variation investigated as well as Commercial Heat 2 – SA in the form of box and whisker plots. A schematic for interpreting the box and whisker plots is provided in Figure 28. The maximum room-temperature hardness for UNS S31025 permitted in ASTM A213 and SA-213 is shown in Figure 27 by the dashed horizontal lines. The following were observed:

- There is a spike in hardness seen in the sample that was PT at 800°C for 9 hours
- Samples that were PT at 750°C for 3 hours and 9 hours show lower hardness values compared to the other precipitation treatment variations investigated

- All the precipitation treatment variations investigated met the room-temperature hardness requirement specified in ASTM A213 and SA-213 for UNS S31025 except a specimen treated at 800℃ for 9 hours.

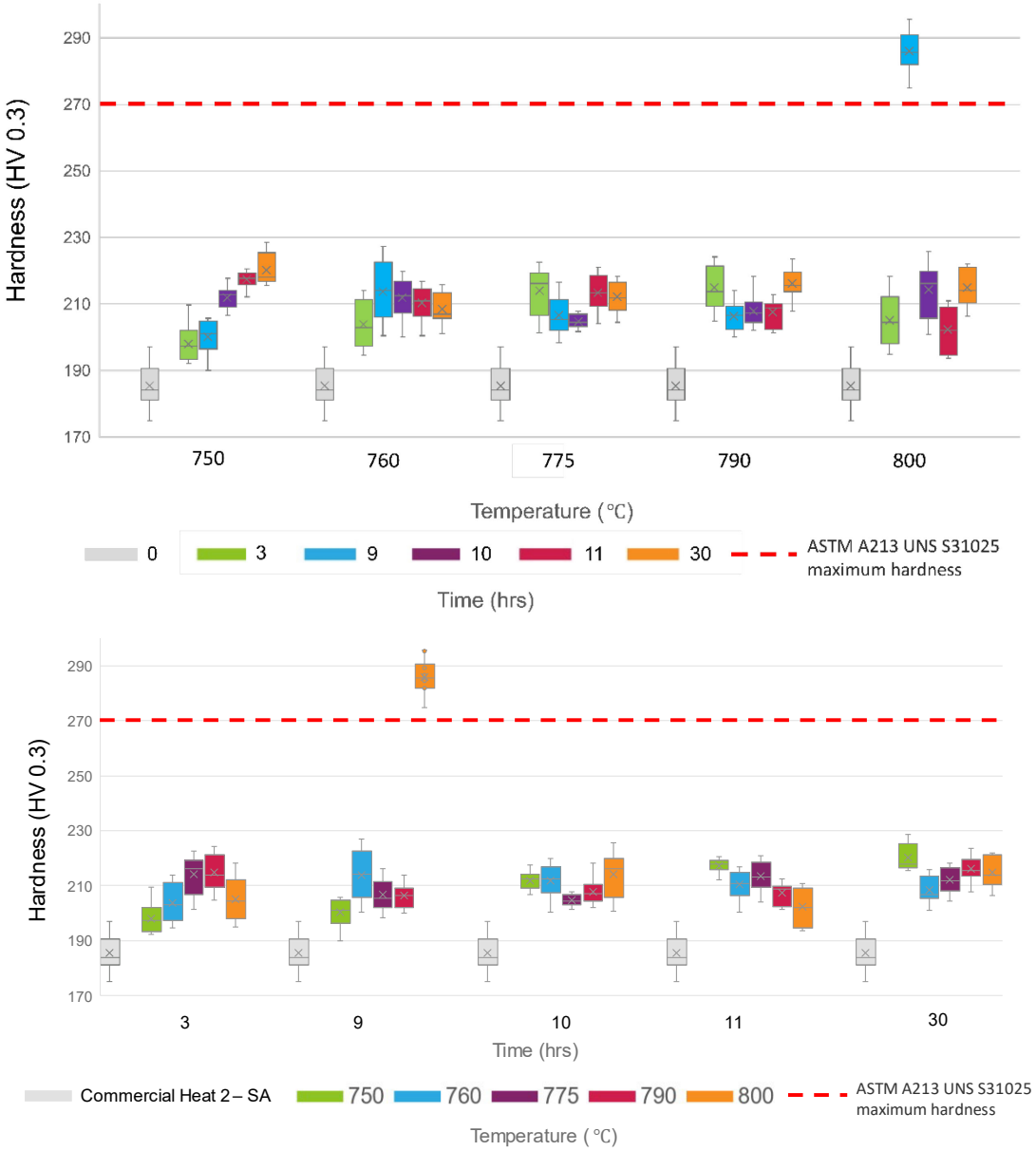

Figure 27. Box and whisker plots of the hardness measured for Commercial Heat 2 – SA and each Commercial Heat 2 precipitate treatment variation investigated. The top image groups the data by precipitation treatment temperature while the bottom bar plot groups the data by the length of the precipitation treatment. The red dashed horizontal lines are the maximum room-temperature hardness for UNS S31025 permitted in ASTM A213 and SA-213.

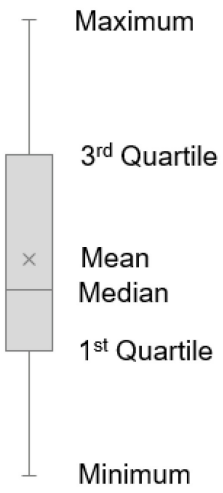

Figure 28. Schematic for interpreting the box and whisker plot.

The repeatability of the first two trends described above were investigated using Commercial Heat 1. A total of three precipitation treatments were repeated to investigate the spike in hardness observed in the specimen precipitate treated at 800°C for 9 hours: (a) 800°C for 3 hours; (b) 800°C for 9 hours; and (c) 800°C for 10 hours. The results are presented in Figure 29 and compared with those from Commercial Heat 2. It is apparent the spike in hardness values observed in Commercial Heat 2 for the precipitation treatment conducted at 800°C for 9 hours was not replicated in Commercial Heat 1.

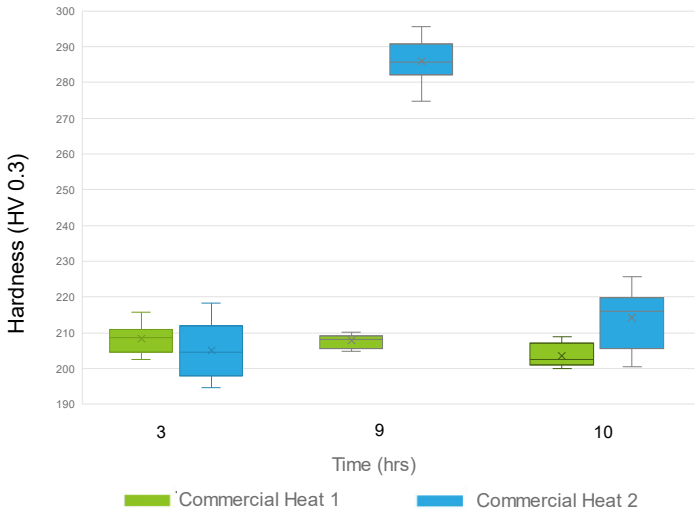

Figure 29. Box and whisker plots of the hardness measured as a function of time for precipitation treatments conducted at 800°C for Commercial Heats 1 and 2.

A total of four precipitation treatments were repeated with Commercial Heat 1 to investigate the increase in hardness observed at 750°C between 9 and 10 hours: (a) 750°C for 3 hours; (b) 750°C for 9 hours; (c) 750°C for 10 hours; and (d) 750°C for 11 hours. The hardness measured for these precipitate

treatment variations in Commercial Heats 1 and 2 are shown in Figure 30. From this figure, it is apparent the increase in hardness at 750°C between 9 and 10 hours observed in Commercial Heat 2 was not repeated in Commercial Heat 1; the hardness measured in Commercial Heat 1 remained constant for the four precipitate treatment variations investigated. It should be noted the time-temperature-transformation (TTT) diagram shown in Figure 31 indicates that the hardness increase observed in Commercial Heat 2 may be correlated with the transformation of the $M_{23}C_6$ precipitate (Zhang, Sham, and Young 2019).

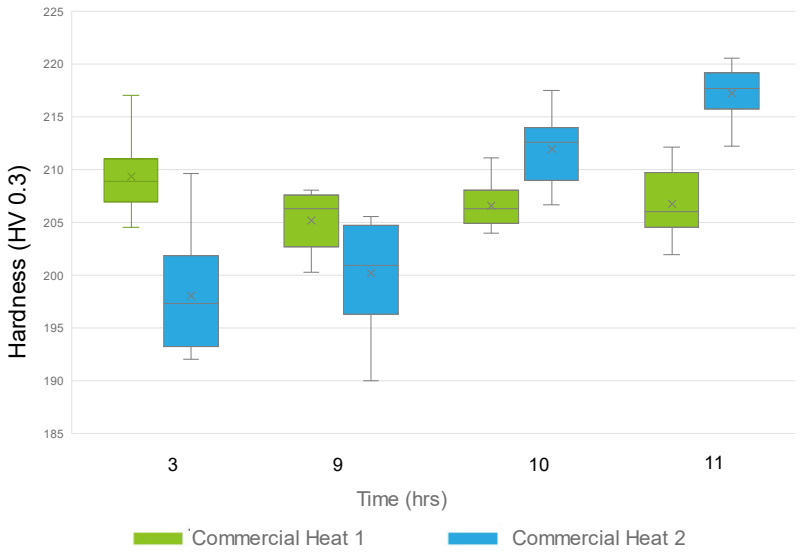

Figure 30. Box and whisker plots of the hardness measured as a function of time for precipitation treatments conducted at 750°C for Commercial Heats 1 and 2.

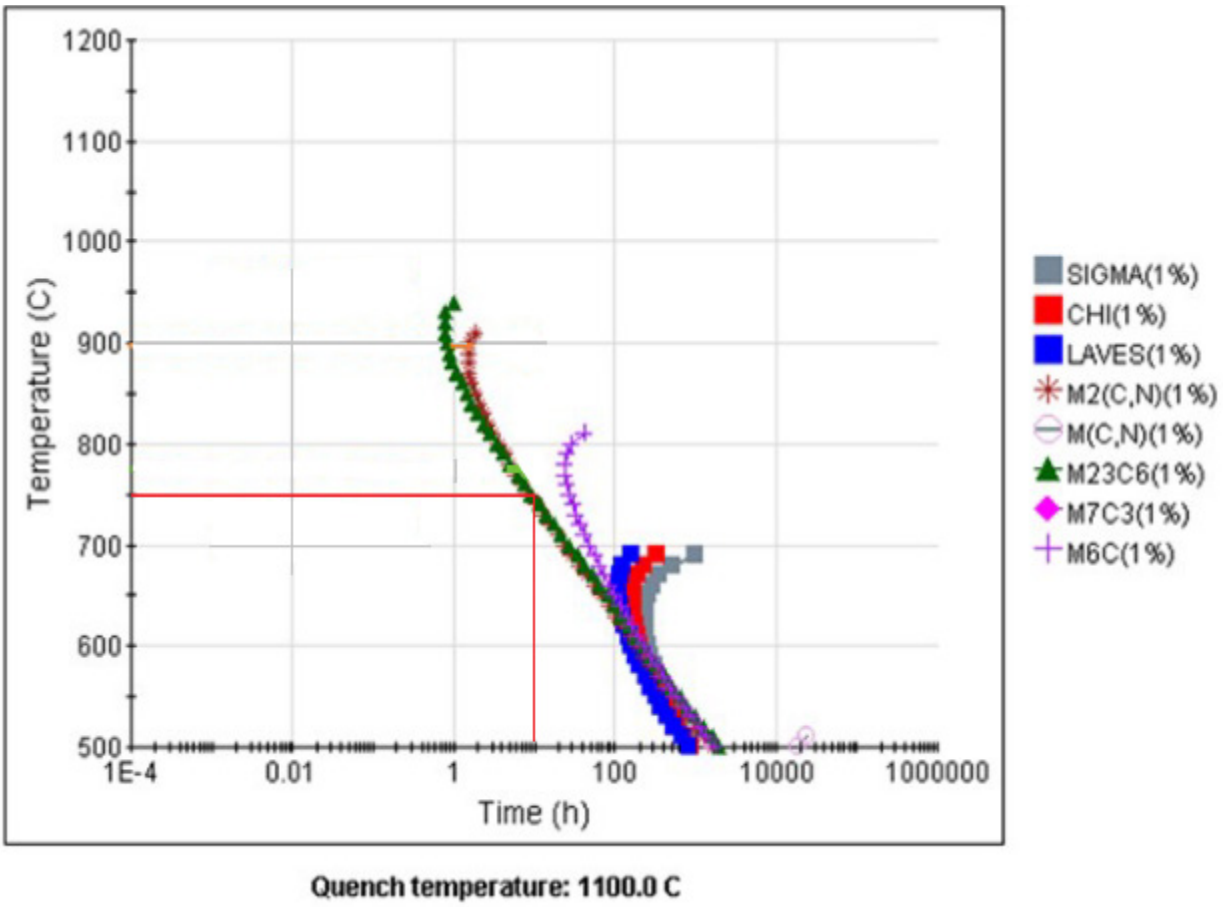

Figure 31. TTT diagram for A709 for 1% transformation. Modeling used the Carlson Heat with the ESR final processing step and SA at 1100°C as its input. The red lines indicated the 1% transformation of $M_{23}C_6$ after 9 hours at 750°C. The figure has been modified from the following reference (Zhang, Sham, and Young 2019).

Apart from the Commercial Heat 2 specimen that was PT at 800°C for 9 hours, all of the precipitation treatment variations investigated satisfy the room-temperature hardness requirement specified in ASTM A213 and SA-213 for UNS S31025. The hardness measured for the Commercial Heat 2 specimen that was PT at 800°C for 9 hours is considered an outlier. The next step is to look at the extremes of the precipitation treatment variations investigated and conduct elevated-temperature mechanical testing. The purpose of this testing would be to assess if these time and temperature variations have any impact on the mechanical performance.

6. SUMMARY

Work was conducted at INL in FY 2022 associated with A709 precipitates to support the A709 Code Cases. This work encompassed two broad goals: (a) Understand the microstructure of Commercial Heat 2 and determine if the precipitates seen in this heat are comparable with those found in Commercial Heat 1; and (b) Understand the impact of variations in the time and temperature of the precipitation treatment for A709.

The precipitates present in Commercial Heat 2 – SA and Commercial Heat 2 – PT were characterized using TEM. Direct comparisons were made between the following: (a) Commercial Heat 1 – SA and Commercial Heat 2 – SA; (b) Commercial Heat 1 – PT and Commercial Heat 2 – PT; and (c) Commercial

Heat 2 – SA and Commercial Heat 2 – PT. Comparable MX precipitates were seen in both Commercial Heat 1 – SA and Commercial Heat 2 – SA. However, the large 1.5 μm precipitates, Nb-rich MZ or Z-phase precipitates, and $M_{23}C_6$ precipitates on the grain boundaries were only seen in Commercial Heat 2 – SA. Similarly, $M_{23}C_6$ precipitates as well as MX or Z-phase precipitates of comparable size and composition were seen in Commercial Heat 1 – PT and Commercial Heat 2 – PT. Chains of $M_{23}C_6$ precipitates, however, were only seen in Commercial Heat 1 – PT. $M_{23}C_6$ precipitates were present at the grain boundaries, twin boundaries, and within the grain interiors for Commercial Heat 2 – PT but were only observed at the grain boundaries for Commercial Heat 2 – SA. However, the density of the $M_{23}C_6$ precipitates at the grain boundaries was significantly higher in Commercial Heat 2 – PT compared to Commercial Heat 2 – SA. Nanosized MX or Z-phase precipitates were seen in the grain interior for both Commercial Heat 2 – SA and Commercial Heat 2 – PT. The density of these precipitates was significantly larger in Commercial Heat 2 – PT.

Both Commercial Heat 2 – SA and Commercial Heat 2 – PT were observed to have $M_{23}C_6$ precipitates and MX precipitates present at the grain boundaries. The density of the MX precipitates remained the same between the two conditions. However, the density of the $M_{23}C_6$ precipitates was significantly higher in Commercial Heat 2 – PT. The $M_{23}C_6$ precipitates were observed at the grain boundaries, twin boundaries, and within the grain interior for Commercial Heat 2 – PT. While in Commercial Heat 2 – SA, the $M_{23}C_6$ precipitate is only present at the grain boundaries. Nanosized MX or Z-phase precipitates were seen in both conditions.

The impact of variations in the time and temperature of the precipitation treatment on the properties of A709 was investigated in Commercial Heat 2 through hardness measurements. The precipitation treatment temperature was varied from 750℃ to 800℃ for times ranging from 3 hours to 30 hours. The following were observed in Commercial Heat 2: (a) a spike in hardness occurred in the specimen heat treated for 9 hours at 800℃; (b) an increase in hardness was observed between the specimens heat treated for 9 and 10 hours at 750℃; and (c) All of the precipitation treatment variations investigated met the room-temperature hardness requirement specified in ASTM A213 and SA-213 for UNS S31025, except a specimen PT at 800℃ for 9 hours. The first two observations were not replicated when investigated using Commercial Heat 1. The hardness measured for the Commercial Heat 2 specimen that was PT at 800℃ for 9 hours is considered an outlier. The next step is to look at the extremes of the precipitation treatment variations investigated and conduct elevated-temperature mechanical testing. The purpose of this testing would be to assess if these time and temperature variations have any impact on the mechanical performance.

7. REFERENCES

ASME International. 2021a. "Section III, Division 5: Rules for Construction of Nuclear Facility Components, High Temperature Reactors." In ASME Boiler and Pressure Vessel Code: An International Code. ASME. New York, NY.

ASME International. 2021b. "Standard Specification for Seamless Ferritic and Austenitic Alloy-Steel Boiler, Superheater, and Heat Exchanger Tubes." ASME SA-213/SA-213M. New York, NY.

ASME International. 2021c. "20Cr-25Ni-1.5Mo-Cb-N Seamless Austenitic Stainless Steel Tube, Section I." Case 2581. New York, NY.

ASTM International. 2017a. "Standard Test Methods for Vickers Hardness and Knoop Hardness of Metallic Materials." ASTM E92-17. West Conshohocken, PA.

ASTM International. 2017b. "Standard Test Method for Microindention Hardness of Materials." ASTM E384-17. West Conshohocken, PA.

ASTM International. 2021d. "Standard Test Methods for Tension Testing of Metallic Materials." ASTM E8/E8M-21. West Conshohocken, PA.

Executive Order No. 14,008. 2021. 3 C.F.R 7624. "Tackling the Climate Crisis at Home and Abroad." January 27, 2021.

Ding, Rengen, Jin Yan, Hangyue Li, Suyang Yu, Afsaneh Rabiei and Paul Bowen. 2019. "Microstructural Evolution of Alloy 709 During Aging." Materials Characterization 154: 400-423. https://doi.org/10.1016/j.matchar.2019.06.018.

Idaho National Laboratory. 2022a. "Precipitation Treatment of Alloy 709." PLN-6567 INL/MIS-22-66482-Rev000, Idaho National Laboratory.

Idaho National Laboratory. 2022b. "Precipitation treatment of Alloy 709 with Variations in Time and Temperature." PLN-6639 INL/MIS-22-22-68324-Rev000, Idaho National Laboratory.

Idaho National Laboratory. 2022c. "Hardness Testing." PLN- 6649 INL/MIS-22-68389-Rev000, Idaho National Laboratory.

McMurtrey, Michael. 2018. "Report on the FY-2018 Creep Rupture and Creep-Fatigue Tests on the First Commercial Heat of Alloy 709." INL/EXT-18-46140-Rev000, Idaho National Laboratory. https://doi.org/10.2172/1484686.

McMurtrey, Michael and Ryann Rupp. 2019. "Report on FY-2019 Scoping Creep and Creep-Fatigue Testing on Heat Treated Alloy 709 Base Metal." INL/EXT-19-55502-Rev000, Idaho National Laboratory.

Natesan, Krishnamurti, Xuan Zhang, Ting-Leung Sham, and Hong Wang. 2017. "Report on the Completion of the Procurement of the First Heat of Alloy 709." ANL-ART-89, Argonne National Laboratory. https://doi.org/10.2172/1364649.

Natesan, Krishnamurti, Xuan Zhang, and Meimei Li. 2018. "Report on the initiation of planned FY18 short and intermediate term creep rupture tests and creep-fatigue tests on the first Commercial Heat of Alloy 709." ANL-ART-51, Argonne National Laboratory. https://doi.org/10.2172/1485134.

Nuclear Regulatory Commission. 2022. "Acceptability of ASME Code Section III, Division 5, High Temperature Reactors." NRC-2021-0117. 87 Fed. Reg. 11,490. March 1, 2022.

O'Donnell, William J. and Donald S. Griffin. 2007. "Regulatory Safety Issues in the Structural Design Criteria of ASME Section III Subsection NH and for Very High Temperatures for VHTR & GEN IV." DOE/ID14712-2, ASME Standards Technology, LLC. https://doi.org/10.2172/974279.

Rupp, Ryann E. and Michael D. McMurtrey. 2020. “Mechanical Properties of Aged A709.” INL/EXT-20-59630-Rev000, Idaho National Laboratory.

Rupp, Ryann, Yanli Wang, Xuan Zhang and Ting-Leung Sham. 2021. “Integrated FY-2021 Elevated-Temperature Mechanical-Testing Results for Alloy 709 Code Case.” INL/EXT-21-64314-REV000, Idaho National Laboratory.

Sham, Ting-Leung and Krishnamurti Natesan. 2017. “Code Qualification Plan for an Advanced Austenitic Stainless Steel, Alloy 709, for Sodium Fast Reactor Structural Applications.” International Conference on Fast Reactors and Related Fuel Cycles: Next Generation Nuclear for Sustainable Development (FR17), Yekaterinburg, Russia, IAEA-CN-245-74.

Sham, Ting-Leung, Yanli Wang, Ryann Bass, and Xuan Zhang. 2022. “A709 Qualification Plan Update and Mechanical Properties Data Assessment.” INL/RPT-22-67641, Idaho National Laboratory.

Song, Rongjie, Caleb D. Clement, Michael D. McMurtrey. 2021. “Characterization of Alloy 709 Commercial Heats.” INL EXT-21-64284-REV000, Idaho National Laboratory.

Thomas, Brian E. 2018. “NRC Response to ASME Letter of Request for NRC Endorsement of ASME Boiler and Pressure Vessel Code, Section III, Division 5”. ML18211A571, United States Nuclear Regulatory Commission.

Wang, Hong, C. Shane Hawkins, Eric C. Disney, and Jeremy L. Moser. 2018. “The Initiation of Long-Term Creep Rupture Tests on the First Alloy 709 Commercial Heat.” ORNL/TM-2018/985, Oak Ridge National Laboratory. https://doi.org/10.2172/1476397.

Wright, Richard N. 2020. “Report Documenting Activity for Second Alloy 709 Commercial Heat.” INL/EXT-20-59880-Rev000, Idaho National Laboratory.

Zhang, Xuan, Ting-Leung Sham, and George A. Young. 2019. “Microstructural Characterization of Alloy 709 Plate Materials with Additional Heat Treatment Protocol.” ANL-ART-170, Argonne National Laboratory. https://doi.org/10.2172/1601459.

Zhang, Xuan, and Ting-Leung Sham. 2020. “Report on the FY20 Characterization of Age Hardened Alloy 709 Materials.” ANL-ART-192, Argonne National Laboratory. https://doi.org/10.2172/1656611.

Zhang, Xuan, Ting-Leung Sham, and Meimei Li. 2021. “Deformation Mechanism of Aged Hardened Alloy 709 Materials.” ANL-ART-233, Argonne National Laboratory. https://doi.org/10.2172/1810715.

Page intentionally left blank

Appendix A
Hardness Data from Commercial Heat 1 and Commercial Heat 2

Table 6. Precipitation treatment Vickers hardness data (HV 0.3) for Commercial Heat 1.

Temperature	Time	Vickers hardness (HV 0.3)									
(°C)	(hours)	1/2 thickness					1/4 thickness				
		1	2	3	4	5	1	2	3	4	5
750	3	212.5	209.1	207.1	210.5	204.5	208.7	206.5	209.2	217	208.6
750	9	206.5	203.5	208.1	207.5	207.9	206.9	202.9	200.3	206.1	202
750	10	205	211.1	207.9	207	206.5	206.1	205.3	204.6	204	208.6
750	11	210.3	209.5	202	205.2	205.9	206.1	208.7	212.1	205.8	202.4
800	3	215.9	211.2	207	210.5	210.9	206.4	210.8	204	202.7	204.9
800	9	205.8	204.9	208.1	205.3	210.2	207.6	210.3	208.9	208.3	208.5
800	10	207.4	201.3	202.4	200	200.6	202.6	207	208.9	203.7	202.7

Table 7. Precipitation treatment Vickers hardness data (HV 0.3) for Commercial Heat 2.

Temperature	Time	Vickers hardness (HV 0.3)									
(°C)	(hours)	1/2 thickness					1/4 thickness				
		1	2	3	4	5	1	2	3	4	5
750	3	193.5	198.8	201.7	209.6	192.4	192.1	194.6	199.8	195.8	202.4
760	3	213.8	198.1	195	207.1	194.5	205.4	210.2	198.9	200.4	213.8
775	3	218.5	207.1	205.3	201.2	214.5	213.8	218.7	220.6	222.7	217.8
790	3	204.8	207.9	220.6	224.1	212.6	210	213.8	218.7	222.9	213.6
800	3	200.5	197	194.8	198.7	210.9	212.8	208.6	198.2	218.3	211.7
750	9	204.5	190	198.8	197.9	196.4	203.1	203.9	205.6	196.2	205.6
760	9	214.9	227.1	221.6	225.3	206.1	200.3	205.2	206.7	213.2	216.2
775	9	216.3	198.4	207.9	202.5	203.9	209.8	200.2	206.3	204.6	215.9
790	9	201.7	200.1	206.3	209	202.3	208.5	206.7	213.9	210	204.4
800	9	281.8	282.5	287.8	284.6	295.2	274.7	286.7	282.1	295.6	289.3
750	10	217.5	213.7	213.3	210.3	212.9	212.3	214.9	209.2	206.7	208.3
760	10	209.3	206.3	200.2	218.2	212.1	214.8	219.8	212.8	216.3	207.6
775	10	204.5	207.3	203.2	206.6	207.9	203.1	206.1	201.5	203.4	204.6
790	10	218.1	208	206.5	202.1	205.4	202.6	210.3	211.5	205	207.6
800	10	200.6	205.9	217	219.4	221.4	216.1	216	225.6	205.3	214.8
750	11	220.1	212.2	220.50	217.6	218.8	216.6	218.6	213	217	217.8
760	11	200.4	209.5	215.8	214.3	216.7	212.7	210.2	205.1	206.8	211.3
775	11	213.4	220.8	215.7	209.7	208.7	204.2	221	210.2	217.8	213.1
790	11	202.2	201.2	209.3	202.3	208.2	209.5	212.6	210.4	209.7	208
800	11	193.7	200.9	203.3	194.7	208.8	194.3	199.3	209.4	207.7	210.8
750	30	216.9	216.3	218.6	228.5	217.2	224.6	215.5	220.1	227.7	216.8
760	30	209.6	206.8	202.8	200.9	215.4	215.7	206.4	206.5	212.7	206.9
775	30	218.3	217.9	216	204.5	213.7	209.3	207.3	208.2	210	215.7
790	30	219	215.1	215.3	218.7	207.7	221.1	215.5	215.7	223.5	208.7
800	30	221.9	214	211.2	206.4	221.6	213.5	218.7	213.6	220.9	207.9

Table 8. Vickers hardness data (HV 0.3) for Commercial Heat 2 – SA taken from a previous study. Note that this data has not been taken in accordance with PLN-6649 (INL2022c).

	Vickers hardness (HV 0.3)											
	1/2 thickness						1/4 thickness					
	1	2	3	4	5	6	1	2	3	4	5	6
Commercial heat 2 - SA	175	181	194	193	197	184	180	184	183	186	181	188

Appendix B
Time and Temperature Recordings During the Heat Treatments

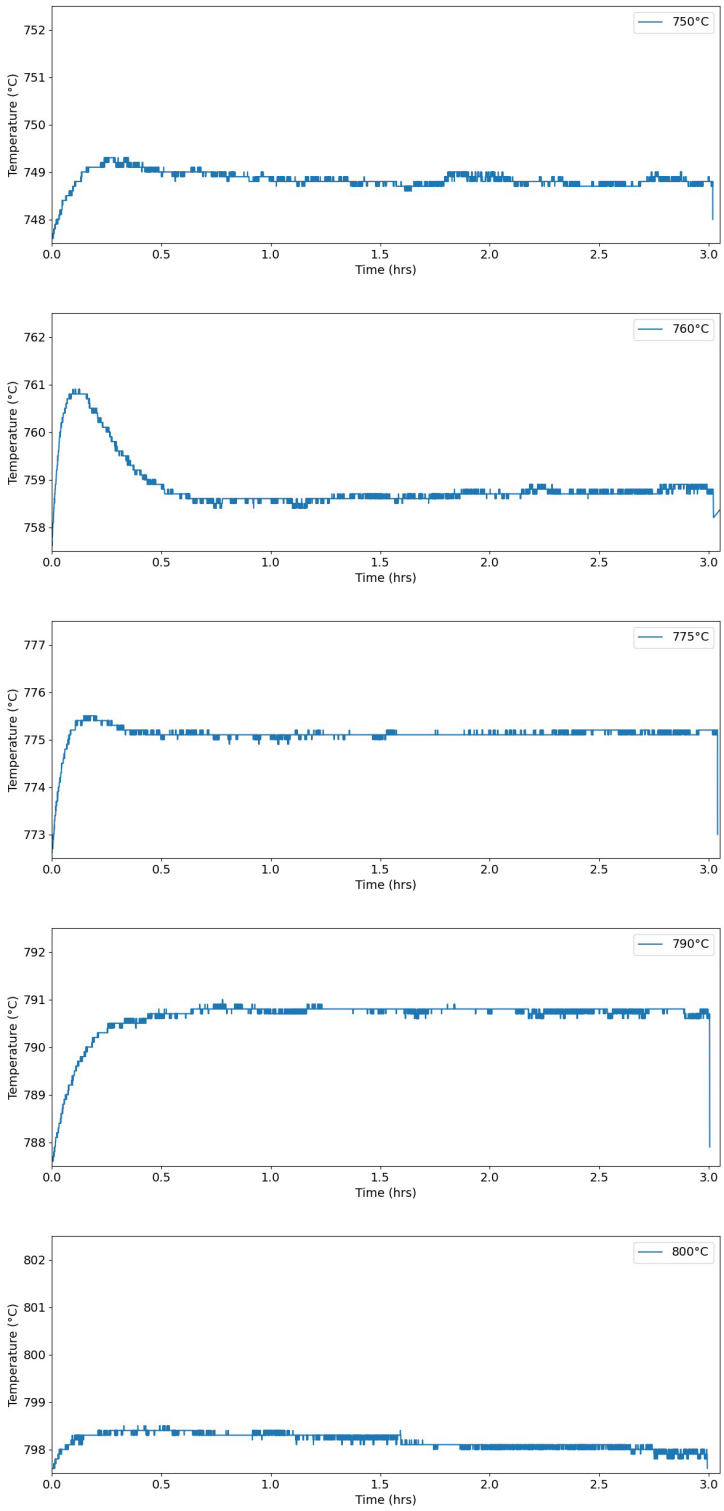

Figure 32. Time at temperature for the 3-hour precipitation treatments of Commercial Heat 2 at 750, 760, 775, 790 and 800°C.

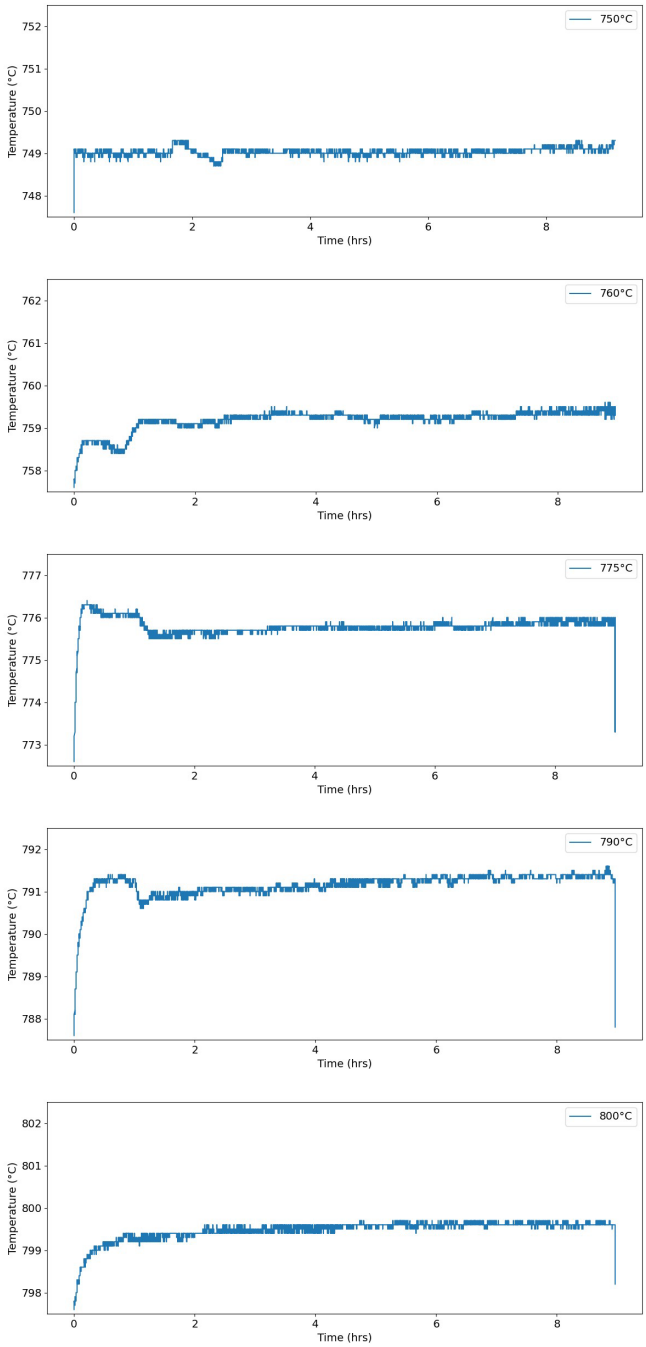

Figure 33. Time at temperature for 9-hour precipitation treatment of Commercial Heat 2 at 750, 760, 775, 790 and 800°C.

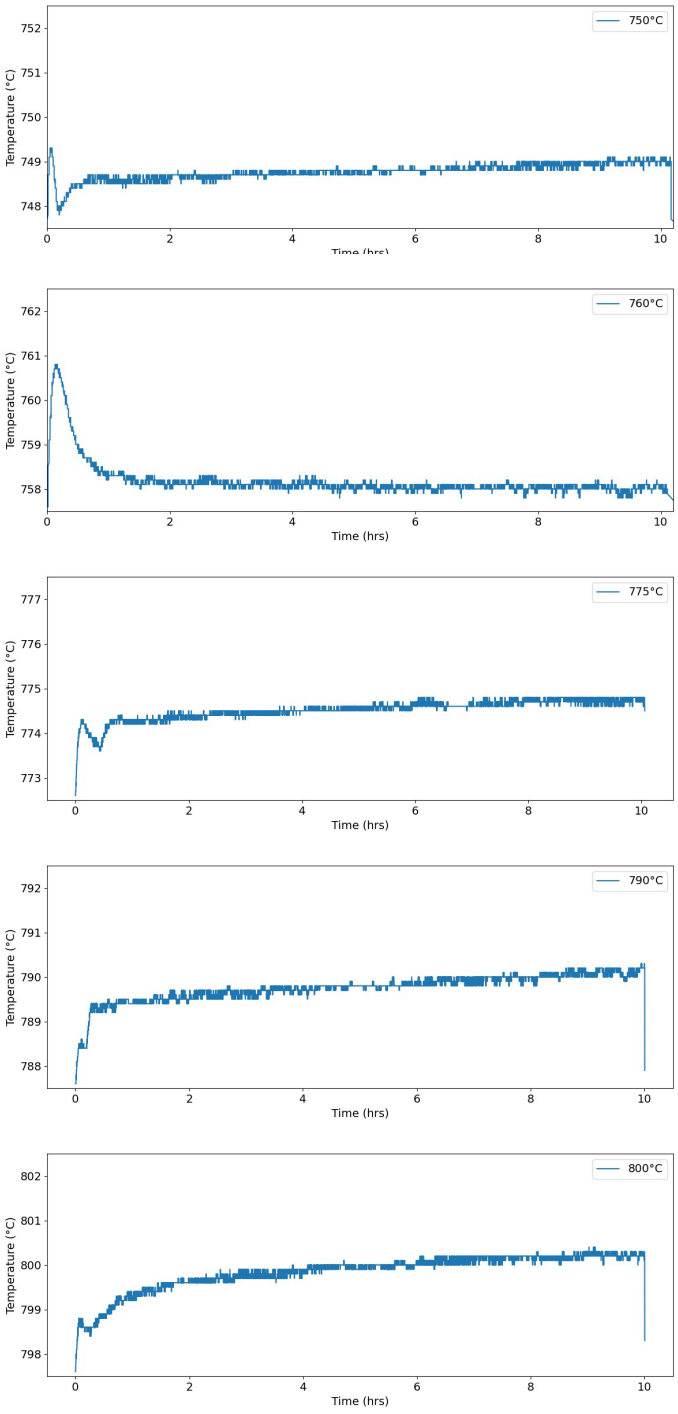

Figure 34. Time at temperature for 10-hour precipitation treatment of Commercial Heat 2 at 750, 760, 775, 790 and 800°C.

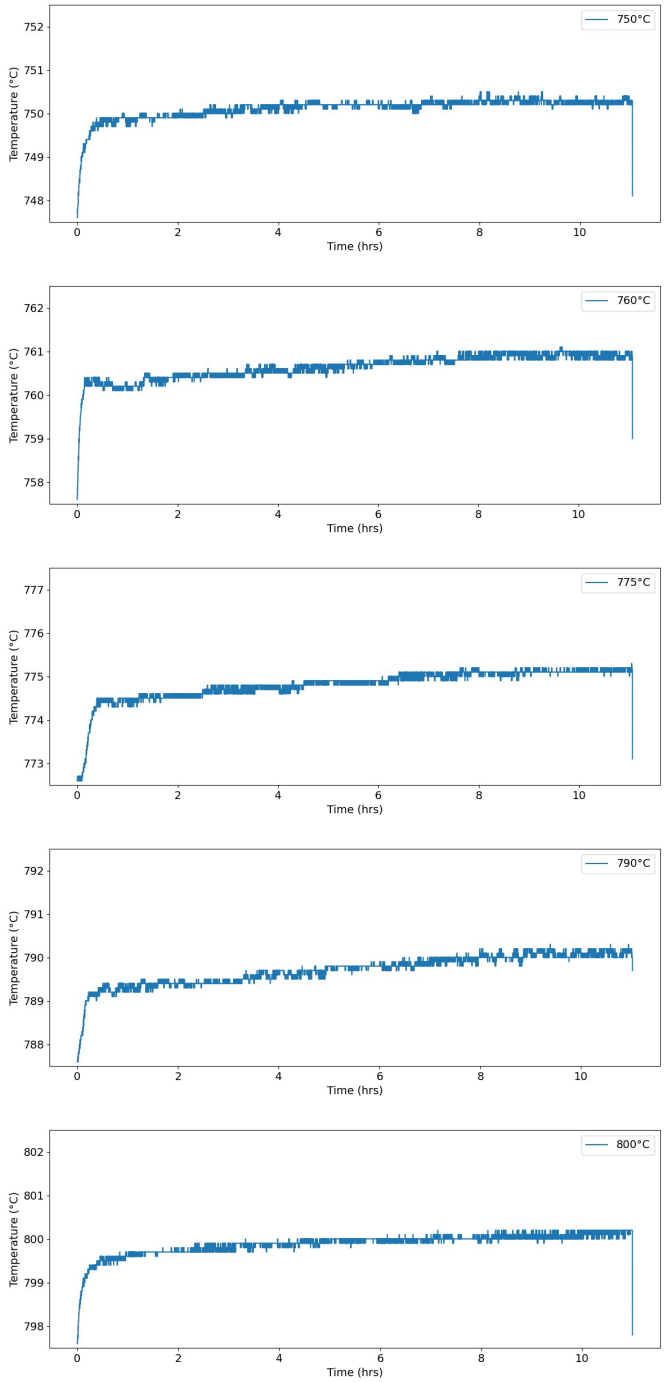

Figure 35. Time at temperature for 11-hour precipitation treatment of Commercial Heat 2 at 750, 760, 775, 790 and 800°C.

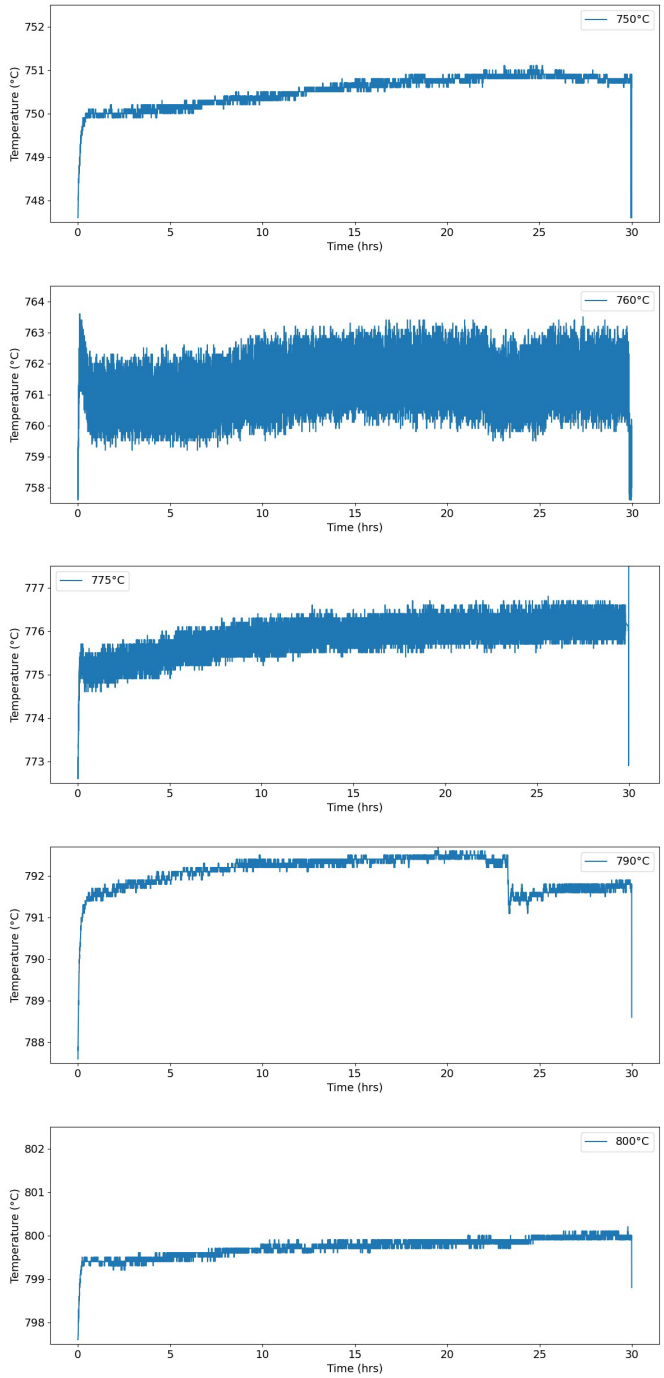

Figure 36. Time at temperature for 30-hour precipitation treatment of Commercial Heat 2 at 750, 760, 775, 790 and 800°C.

It should be noted that a temperature of 763.5°C was recorded for the sample PT at 760°C for 30 hours. This exceeds the permissible 2.5°C window set in PLN-6567. This temperature deviation is considered insignificant and is not anticipated to negatively impact the results.

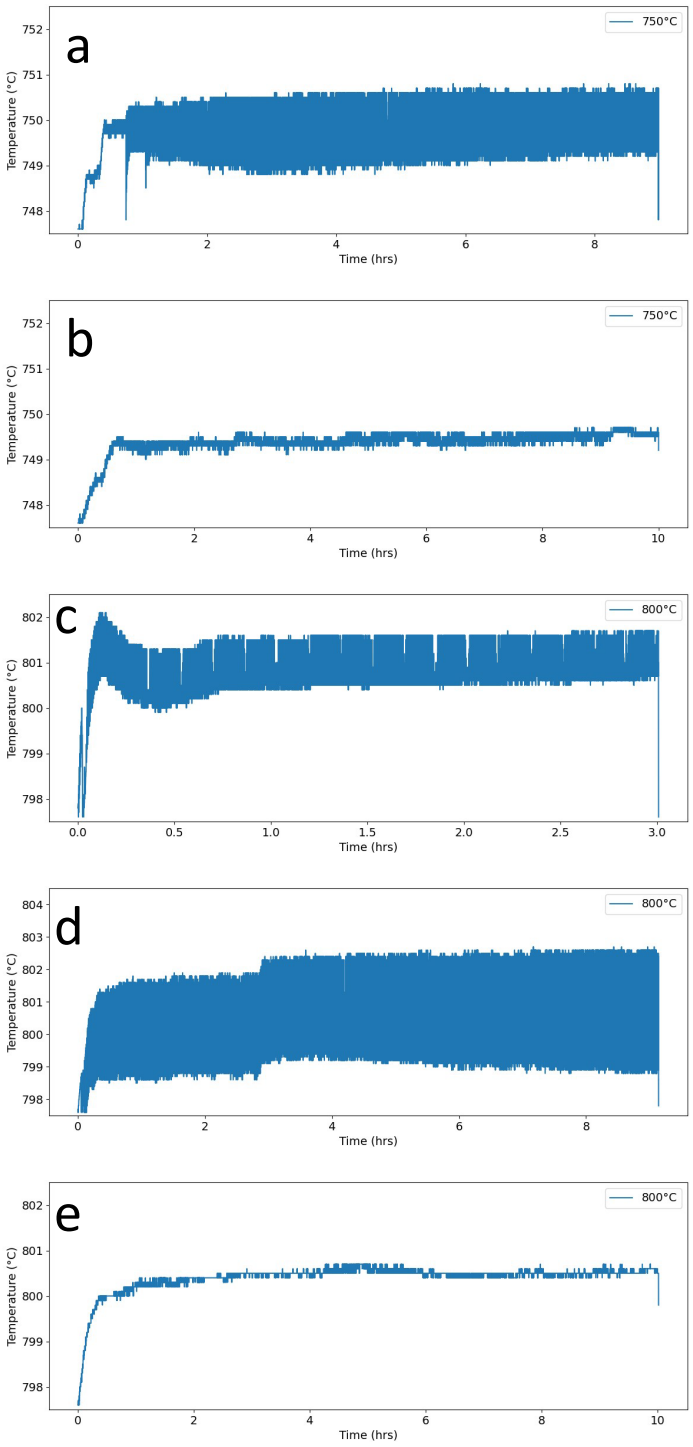

Figure 37. Time at temperature for Commercial Heat 1 for (a) 750°C for 9 hours, (b) 750°C for 10 hours, (c) 800°C for 3 hours, (d) 800°C for 9 hours, and (e) 800°C for 10 hours.

It should be noted that a temperature of 802.5°C was recorded for the sample PT at 800°C for 9 hours. This exceeds the permissible 2.5°C window set in PLN-6567. This temperature deviation is considered insignificant and is not anticipated to negatively impact the results.